

The impact of helium reionization on the structure of the intergalactic medium

Avery Meiksin^{1*}, Eric R. Tittley¹

¹*SUPA†, Institute for Astronomy, University of Edinburgh, Blackford Hill, Edinburgh EH9 3HJ, UK*

Accepted . Received ; in original form

ABSTRACT

We examine the impact of helium reionization on the structure of the intergalactic medium (IGM). We model the reionization using a radiative transfer (RT) code coupled to the combined gravity hydrodynamics code *Enzo*. Neutral hydrogen and helium are initially ionized by a starburst spectrum, which is allowed to gradually evolve into a power law spectrum over the redshift interval $3.0 < z < 4.0$. The temperature-density relation of the gas is found to fan out and flatten following HeII reionization, with an inversion for high overdensities of $\rho/\langle\rho\rangle > 5$. Peculiar velocities of up to 10 km s^{-1} are induced by the increased pressure, with the gas density field distorted over large coherent regions by 10–20 per cent., and the dark matter by levels of 1 per cent. The photoionization-induced flows may thus distort the matter power spectrum at comoving wavenumbers $k > 0.5 h \text{ Mpc}^{-1}$ by a few per cent. by $z = 2$.

Absorption spectra for H I and He II are drawn from the simulations, and absorption lines are fit to the spectra. The increased temperature following He II reionization reduces the line centre optical depths, resulting in an enhancement in the fraction of very low optical depth pixels and an overall distortion in the pixel flux distribution compared with He II reionization in the optically thin limit. A median Doppler parameter of 35 km s^{-1} is obtained for the H I absorption systems at $z = 3$. Dividing into subsamples optically thick and optically thin at line centre reveals that the optically thick systems undergo only mild evolution while the optically thin systems evolve rapidly following He II reionization. A comparison between He II and H I absorption features shows a broad distribution in the He II and H I column density ratio, peaking near the measured value and only slightly narrower than measured. The distribution of the ratio of He II and H I Doppler parameters peaks midway between the thermally broadened and velocity broadened limits. A comparison with approximate simulation methods based on either a pseudo-hydrodynamical scheme or a non-RT hydrodynamical simulation with boosted He II heating rate shows moderately good agreement in the absorption line properties, but not to the precision to which they may be measured, and not over the full redshift range for which the high redshift Ly α forest is observed.

Key words: radiative transfer – quasars: absorption lines – quasars: general – cosmology: large-scale structure of Universe – methods: N-body simulations

1 INTRODUCTION

Cosmological simulations of the intergalactic medium (IGM) in the context of cold dark matter (CDM) theories for structure formation have proven extremely successful in reproducing many of the observed properties of the IGM as measured through the Ly α forest. The mean H I transmission through the IGM is recovered for an H I ionizing background

matching that of the measured Quasi-Stellar Object (QSO) luminosity function for $z < 3$, although an enhanced radiation field, likely due to galaxies, is required at higher redshifts. Once normalised to the mean transmission, the H I column density distribution is broadly recovered as well for a Λ CDM model, as is the measured power spectrum of the H I flux. See Meiksin (2009) for a review.

Despite these successes, some of the statistics still show lack of agreement with measured values. Prominent among these is the line widths of the H I absorption features, which tend to be broader than the predictions (Bryan & Machacek

* E-mail: A.Meiksin@ed.ac.uk (AM)

† Scottish Universities Physics Alliance

2000; Theuns et al. 2000). A detailed comparison with measured spectra reveals that the disagreement is among the optically thin Ly α systems, for which an additional contribution of $10 - 15 \text{ km s}^{-1}$, added in quadrature to the Doppler parameter, is required, while the widths of the optically thick systems well match the measured values (Meiksin et al. 2001). One possible explanation is recent heat input at $z \lesssim 4$ into the IGM. The additional required broadening corresponds to a temperature increase of $17 \times 10^3 \text{ K}$. The optically thin systems are associated with moderate density or even underdense structures for which the time to reach thermal equilibrium exceeds a Hubble time (Meiksin 1994; Miralda-Escudé & Rees 1994). The optically thin systems may thus retain a memory of recent heat input at $z \lesssim 4$.

The most likely source of heating is HeII reionization. The abundance of QSOs suggests they would have ionized HeII at a redshift $3 < z_{\text{HeII}} < 4.5$, although possibly as early as $z_{\text{HeII}} \simeq 5$ for sufficiently hard spectra (Meiksin 2005). Support for recent HeII reionization has been based on measurements of the HeII Ly α optical depth of the IGM. The measurements span the redshift range $2.2 < z < 3.8$ based on *Hubble Space Telescope* (*HST*) observations of Q0302–003 ($z_{\text{em}} \simeq 3.3$) (Jakobsen et al. 1994; Heap et al. 2000), *Hopkins Ultraviolet Telescope* and *Far Ultraviolet Spectroscopic Explorer* (*FUSE*) observations of HS 1700+6416 ($z_{\text{em}} \simeq 2.7$) (Davidson et al. 1996; Fechner et al. 2006), *HST* and *FUSE* observations of HE 2347–4342 ($z_{\text{em}} \simeq 2.9$) (Reimers et al. 1997; Kriss et al. 2001; Smette et al. 2002; Shull et al. 2010), and *HST* observations of PKS 1935–692 ($z_{\text{em}} \simeq 3.2$) (Anderson et al. 1999), SDSS J2346–0016 ($z_{\text{em}} \simeq 3.5$) (Zheng et al. 2004, 2008), Q1157+3143 ($z_{\text{em}} \simeq 3.0$) (Reimers et al. 2005) and SDSS J1711+6052 ($z_{\text{em}} \simeq 3.8$) (Zheng et al. 2008). The HeII Ly α optical depths rise rapidly from $\tau_{\text{HeII}} \simeq 1.00 \pm 0.07$ averaged over the redshift interval $z = 2.2 - 2.6$ to $\tau_{\text{HeII}} \simeq 4.9$ at $z \simeq 3.3$ (Syphers et al. 2011), as if entering into the epoch of HeII reionization.

The origin of the UV background, however, is still not well established. The high HeII Ly α optical depths compared with the corresponding values found for H I generally requires that the UV metagalactic background be soft between the HeII and H I photoelectric edges, with a ratio of H I to HeII photoionization rates of $\Psi > 200$ at $z \approx 3$ (Madau & Meiksin 1994), corresponding to a source spectral index for $f_\nu \sim \nu^{-\alpha_S}$ of $\alpha_S > 1.8$ after allowing for the filtering of the radiation through the IGM (Madau & Meiksin 1994; Haardt & Madau 1996; Bolton et al. 2006). This is consistent with the inferred spectral index of bright high redshift ($0.3 < z < 2.3$) QSOs after correcting for IGM absorption (Telfer et al. 2002), but it is inconsistent with the much harder spectra found for dimmer QSOs nearby ($z < 0.67$) (Scott et al. 2004), for which minimal IGM corrections are required. Possibly ionizing radiation from galaxies boosts the H I photoionization rate, however the contribution from QSOs alone approximately matches the required rate to recover the measured H I Ly α optical depth (Meiksin 2005; Bolton et al. 2005), leaving little room for additional sources.

The optical depth measurements are moreover found to fluctuate over a wide range at a given redshift. This is most dramatically illustrated by measurements of the HeII Ly α forest compared with the corresponding measurements

of H I. A wide spread is found for the column density ratio $\eta = N_{\text{HeII}}/N_{\text{HI}}$, varying at least over the range $4 < \eta < 600$ at $2.3 < z < 2.8$ (Zheng et al. 2004; Reimers et al. 2005; Fechner et al. 2006; Shull et al. 2010). The higher values correspond to H I to HeII photoionization rate ratios of $\Psi > 1000$. Such fluctuations are expected during the epoch of HeII reionization, so that the large HeII Ly α optical depth values may result from a mean over regions in which most of the helium is still in the form of HeI.

The interpretation is not unique, however. Due to the discreteness of the sources of ionizing radiation and attenuation by the IGM, local fluctuations are expected in the UV metagalactic background (Zuo 1992; Fardal et al. 1998; Meiksin & White 2003). The distribution of fluctuations in η measured in HE 2347–4342 are well matched by a UV background dominated by QSOs with a soft spectral index consistent with the data of Telfer et al. (2002) (Shull et al. 2004; Fardal et al. 1998; Bolton et al. 2006), as are the η fluctuations measured in HS 1700+6416 (Meiksin 2009). Possibly a harder spectrum could be accommodated in the presence of additional H I ionizing sources other than QSOs, but, again, there is not much room to add more sources without overionizing the hydrogen. The full range of fluctuations in the measured values of τ_{HeII} in several QSO lines of sight suggests the epoch of HeII reionization may have completed as recently as $z \simeq 2.9$ (Furlanetto & Dixon 2010; Shull et al. 2010). By contrast, recent attempts to quantify the thermal evolution of the IGM from the H I Ly α forest measured in QSO spectra indicate a rise in the temperature of gas at the mean density for $z \simeq 4$ (Becker et al. 2011), suggesting HeII reionization was becoming widespread at these times. If both interpretations are correct, then HeII reionization was a drawn out process extending over the redshift range $2.9 \lesssim z \lesssim 4.5$.

The purpose of this paper is to investigate the dynamical impact of helium reionization on the structure of the intergalactic medium and its observational signatures. While early simulations of the IGM included helium reionization, they were done in the optically thin limit. Cosmological simulations solving the radiative transfer (RT) equation during helium reionization were restricted to the gravitational component, which was used to scale the baryonic component properties (Tittley & Meiksin 2007; McQuinn et al. 2009). In this paper, we implement radiation hydrodynamics using the algorithm of Bolton et al. (2004) coupled to the gravity-hydrodynamics code **Enzo**¹ (specifically v.1.0.1). The hydrodynamical response of the gas to the boost in heating when radiative transfer is included could result in more rapid photo-evaporation of the gas in small haloes, allowing reionization to occur more rapidly, as well as in observational signatures on the Ly α forest such as increased line broadening due to outflows from the haloes and a decrease in the ratio of gas density to dark matter density. An increase in the gas temperature will also alter the ionization fractions of hydrogen and helium at a given gas density, producing modifications to the column densities of the absorption features, the distribution function of pixel fluxes, and the flux power spectrum, all basic statistics used to quantify the Ly α forest and the predictions of cosmological models for its structure.

¹ Available from <http://lca.ucsd.edu>.

All results are for a flat Λ CDM universe with the cosmological parameters $\Omega_m = 0.24$, $\Omega_b h^2 = 0.022$ and $h = H_0/100 \text{ km s}^{-1} = 0.73$, representing the total mass density, baryon density and Hubble constant, respectively. The power spectrum has spectral index $n = 0.95$, and is normalized to $\sigma_{8h^{-1}} = 0.74$.

This paper is organized as follows. Estimates for the expected IGM temperature boost following HeII reionization are discussed in the next section. The simulations are described in Sec. 3 and the results presented in Sec. 4. The H I and HeII spectral signatures of HeII reionization are presented in Sec. 5. A comparison with approximate simulation methods is provided in Sec. 6. The principal conclusions are summarised in the final section.

2 PHOTOIONIZATION HEATING

A radiation field with its specific energy density locally approximated near the HeII photoelectric edge by $u_\nu = u_L(\nu/\nu_L)^{-\alpha}$ will photoionize the HeII at the rate per HeII ion

$$\Gamma_{\text{HeII}} = \int d\nu \frac{cu_\nu}{h\nu} \sigma_\nu \simeq h^{-1} c \sigma_0 \frac{u_L}{3 + \alpha} \quad (1)$$

where ν_L is the frequency of the HeII Lyman edge and the photoionization cross-section is approximated as $\sigma \simeq \sigma_0(\nu/\nu_L)^{-3}$. The corresponding heating rate per HeII ion is

$$G_{\text{HeII}} = \int d\nu \frac{cu_\nu}{h\nu} (h\nu - h\nu_L) \sigma_\nu \simeq c \sigma_0 \nu_L \frac{u_L}{(2 + \alpha)(3 + \alpha)}. \quad (2)$$

The heating rate per ionization, normalized by the ionization potential, is then $\epsilon_{\text{HeII}} = G_{\text{HeII}}/(h\nu_L \Gamma_{\text{HeII}}) = 1/(2 + \alpha)$. The energy injected into the gas is thus sensitive to the shape of the local ionizing spectrum. A hardened radiation field with $\alpha < 0$ can result in a large amount of energy deposited per ionization.

The spectrum is expected to harden within an ionization front because hard photons are less likely to be absorbed than soft photons above the photoelectric threshold for a given optical depth at the threshold energy. In general, for a column density N the optical depth above the photoelectric threshold of hydrogen or singly ionized helium is $\tau_\nu \simeq \tau_L(\nu/\nu_L)^{-3}$ where $\tau_L = \sigma_0 N$. The photoionization rate per atom/ion may be expressed in terms of the incident radiation density from the source $u_\nu^S = u_L^S(\nu/\nu_L)^{-\alpha_S}$ as

$$\begin{aligned} \Gamma &= \int_{\nu_L}^{\infty} d\nu \exp\left[-\tau_L \left(\frac{\nu}{\nu_L}\right)^{-3}\right] \frac{cu_L^S \sigma_0}{h\nu} \left(\frac{\nu}{\nu_L}\right)^{-(3+\alpha_S)} \\ &= \frac{1}{3} \frac{cu_L^S}{hN} \tau_L^{-\frac{1}{3}\alpha_S} \gamma\left(1 + \frac{1}{3}\alpha_S, \tau_L\right) \end{aligned} \quad (3)$$

where $\gamma(a, x) = \int_0^x dt e^{-t} t^{a-1}$ is the incomplete gamma function. Similarly, the heating rate per atom/ion is

$$\begin{aligned} G &= \int_{\nu_L}^{\infty} d\nu \exp\left[-\tau_L \left(\frac{\nu}{\nu_L}\right)^{-3}\right] \frac{cu_L^S \sigma_0}{h\nu} \left(\frac{\nu}{\nu_L}\right)^{-(3+\alpha_S)} \\ &\quad \times (h\nu - h\nu_L) \\ &= \frac{1}{3} \frac{cu_L^S \nu_L}{N} \tau_L^{-\frac{1}{3}\alpha_S} \end{aligned}$$

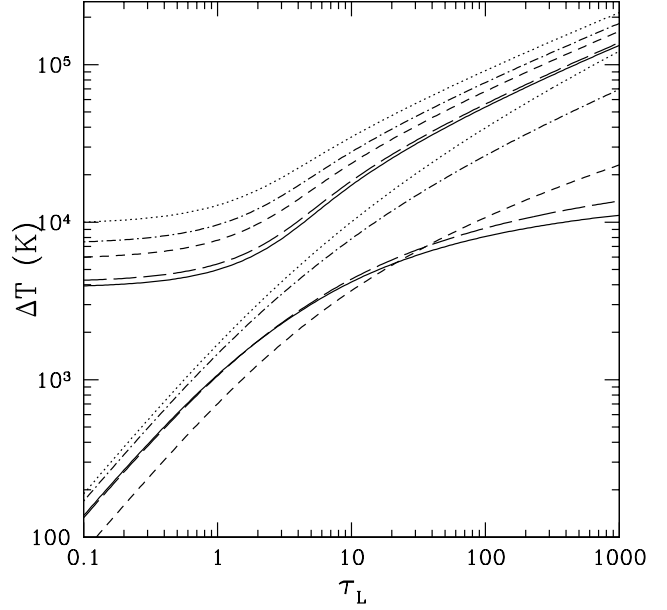


Figure 1. Temperature increment for ionizing HeII to HeIII as a function of the optical depth τ_L at the HeII Lyman edge. Shown for a source spectrum $f_\nu \propto \nu^{-\alpha_S}$ with spectral index $\alpha_S = 1.8$ (solid line), 1.5 (long-dashed line), 0.5 (short-dashed line), 0 (dot-dashed line) and -0.5 (dotted line). The upper set of curves corresponds to reionization going to completion at a fixed optical depth, as would occur for radiation filtered through a foreground absorption system in ionization equilibrium. The temperature boost increases for harder source spectra. For large τ_L , the temperature boost increases like $\tau_L^{1/3}$. The lower set of curves corresponds to the temperature boost for a time varying optical depth as an ionization front sweeps through a slab of material with an initial optical depth $\tau_L(0)$ given by the value τ_L indicated. Very high temperatures are reached for hard spectra.

$$\times \left[\tau_L^{1/3} \gamma\left(1 + \frac{\alpha_S - 1}{3}, \tau_L\right) - \gamma\left(1 + \frac{1}{3}\alpha_S, \tau_L\right) \right]. \quad (4)$$

The resulting heating rate per ionization of HeII will produce a temperature increment

$$\Delta T = \frac{2}{3} \frac{h\nu_L}{k_B} \frac{\epsilon_{\text{HeII}}}{2 \frac{n_{\text{H}}}{n_{\text{He}}} + 3} - \frac{T_i}{2 \frac{n_{\text{H}}}{n_{\text{He}}} + 3}, \quad (5)$$

where T_i is the initial gas temperature and $\epsilon_{\text{HeII}} = G/(h\nu_L \Gamma)$ for HeII. The increment corresponds to the complete ionization of HeII to HeIII at fixed τ_L , as would occur in the presence of an intervening Lyman limit system, already in ionization equilibrium, lying between the source and the region being photoionized if the Lyman limit system dominated the optical depth at the Lyman edge. The radiation field reaching the region being photoionized would be hardened by the absorption within the intervening system. The temperature increment is shown as a function of the optical depth τ_L at the HeII Lyman edge for a range of source spectral indices in Fig. 1 (upper set of curves). A helium mass fraction of $Y = 0.248$ was adopted (Steigman 2007). A system with overdensity $\rho/\langle\rho\rangle$ and comoving thickness L would have an optical depth at the HeII Lyman edge of

$$\tau_{L,\text{HeII}} \simeq 115 \frac{\rho/\langle\rho\rangle}{100} \frac{(1+z)^2}{16} \frac{L}{1 \text{ Mpc}}. \quad (6)$$

The radiation hardening through overdense systems with $\rho/\langle\rho\rangle \sim 200$ and comoving sizes of $0.05 - 0.25$ kpc would produce temperature boosts in the “shadows” they cast in less dense, more quickly photoionized structures, of up to $\Delta T \simeq 40000$ K, and even reaching 10^5 K in the shadows of intervening systems with $\tau_{L,\text{HeII}} > 100$. Radiative recombination and excitation atomic line cooling will subsequently lower the temperature of the gas once the ionization front has passed, although the equilibrium temperature may never be achieved in rarefied underdense regions because of the long required time scales (Meiksin 1994; Miralda-Escudé & Rees 1994).

Alternatively, the heating produced by the passage of an ionization front through a slab of gas in which the optical depth decreases as the ionization front sweeps through may be approximated by equating the incident rate of ionizing photons with the rate at which the gas in the slab is photoionized. For an initial optical depth $\tau_L(0)$ at the Lyman edge, the optical depth at the edge will evolve according to

$$\tau_L(t) = \tau_L(0) \left[1 - k \frac{cu_L^S}{h} \frac{\sigma_0}{\tau_L(0)} t \right], \quad (7)$$

where $k = 1/\alpha_S$ for $\alpha_S > 0$, $k = \log(\nu_{\text{max}}/\nu_L)$ for $\alpha_S = 0$ and $k = [(\nu_{\text{max}}/\nu_L)^{-\alpha_S} - 1]/(-\alpha_S)$ for $\alpha_S < 0$, where ν_{max} is the maximum frequency for which photoionizing photons are produced. Using Eqs. (3) and (4) for the photoionization and heating rates, the number density n of the species undergoing ionization and the thermal energy input per unit volume u , as a function of τ_L , are governed by

$$\frac{d \log n}{d\tau_L} = \frac{1}{3k\tau_L^{1+\alpha_S/3}} \gamma(1 + \frac{\alpha_S}{3}, \tau_L), \quad (8)$$

and

$$\frac{du}{d\tau_L} = -\frac{1}{3} \frac{nh\nu_L}{k\tau_L^{1+\alpha_S/3}} \left[\tau_L^{1/3} \gamma(1 + \frac{\alpha_S - 1}{3}, \tau_L) - \gamma(1 + \frac{\alpha_S}{3}, \tau_L) \right]. \quad (9)$$

The resulting post-ionization temperature is shown in Fig. 1 (lower set of curves). Temperature boosts of $\sim 1000 - 10000$ K are typical, although hard spectra sources ($\alpha_S < 0$) can produce substantially higher temperatures. (Somewhat arbitrarily, $\nu_{\text{max}}/\nu_L = 4$ was assumed for $\alpha_S \leq 0$.) Again, radiative recombination and excitation line cooling will eventually decrease the gas temperature.

Temperature boosts following HeII reionization typically ranging between $\Delta T \simeq 5000 - 20000$ K at $z = 3$, but reaching as high as $\Delta T \simeq 30000 - 40000$ K directly after reionization, were found in the reionization simulations of Tittley & Meiksin (2007) for a source with spectral index $\alpha_S = 0.5$, turning on after a starburst-like spectrum photoionizes the hydrogen and neutral helium to singly-ionized helium. For a pure power-law source spectrum ($\alpha_S = 0.5$) and for a mini-quasar spectrum, lower overall temperatures of $5000 - 20000$ K were obtained at $3 < z < 4$. Higher temperatures were generally found in the denser structures. Temperature boosts of $\Delta T \simeq 10000 - 20000$ K were found by McQuinn et al. (2009) for a QSO spectral distribution with a mean spectral index of $\alpha_S = 1.2$, and boosts of up to $\Delta T \simeq 30000$ K were found for harder source spectra with a mean spectral index $\alpha_S = 0.6$.

In addition to cooling by atomic processes, the gas will undergo adiabatic cooling losses as it escapes from gravitational potential wells that were able to bind the gas when cooler. The expansion velocities will also broaden the absorption features (Meiksin 1994). Previous HeII reionization simulations, which used the dark matter distribution to model the baryon density, were not able to take these effects into account. In this paper, we take the hydrodynamical response of the gas into account by coupling our radiative transfer scheme to a gravity-hydrodynamics code.

3 SIMULATIONS

We have modified the combined hydrodynamics N -body gravity code **Enzo** by replacing its ionization and atomic cooling modules by ones employing the methods used by Tittley & Meiksin (2007). In summary, a probabilistic radiative transfer method is used to compute the reionization of both hydrogen and helium. Atomic cooling from the radiative recombination of the hydrogen and the two helium states is included, along with collisional excitation of neutral hydrogen and Compton cooling. Cooling due to the collisional ionization of hydrogen and the collisional excitation and ionization of helium are negligible for the temperatures encountered in the simulations.

For the hydrodynamical processes at the resolution of cosmological IGM simulations, the dynamical time scales are much longer than the radiative time scales in the vicinity of the ionization front. It would be prohibitively expensive computationally and unnecessary to force the hydrodynamics to evolve at the same time scale as the radiative transfer. Hence, in our implementation the radiative transfer time scale is allowed to drop below that of the hydrodynamics. The energy equation is solved through operator splitting by computing the ionization state of the gas and the amount of photoionization heating and atomic cooling between the hydrodynamical time steps. During the ionization timesteps, all parameters of the gas are taken to be those at the end of the immediately preceding hydrodynamical timestep with the exception of the fluid density and temperature. The density is varied linearly from the previous hydrodynamical timestep to that of the current ionization timestep while the radiative transfer processes along with the gas temperature are evolved on their own, shorter, adaptive time scale.

The simulations were carried out in a box $25h^{-1}$ Mpc (comoving) on a side. This corresponds to the order of the expected size of a HeII ionization front at the helium reionization epoch, when the characteristic diameter of the HeIII zone produced by an individual QSO is comparable to the mean distance between QSOs, which is typically ~ 50 Mpc (comoving) at $z \simeq 3$ (Wolf et al. 2003; Meiksin 2005). Then **Enzo** simulations were performed with 512^3 gravitating particles and 256^3 grid zones for the fluid component, corresponding to a resolution of 98 kpc (comoving), sufficient to resolve the Jeans length.

The incident spectrum corresponds to a hybrid starburst-QSO model as in Tittley & Meiksin (2007): an initial starburst spectrum is turned on at $z = 8$ and transformed into a power-law spectrum $f_\nu \propto \nu^{-0.5}$, turning on the power-law spectrum initially at $z = 4$ and ramping it

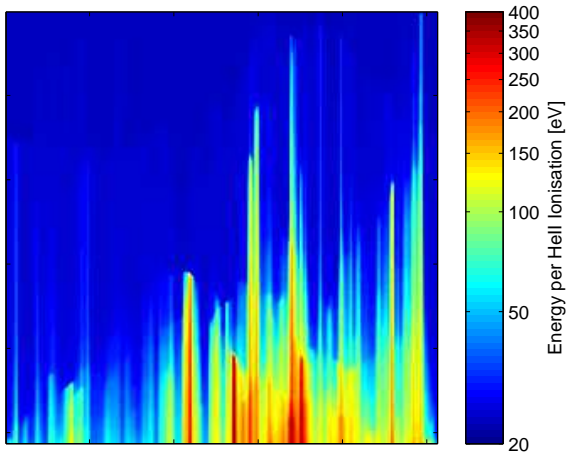


Figure 2. The heating rate per HeII ionization at $z = 3.3$ for a HeII ionization front sweeping across the box from top to bottom.

up to its full value at $z = 3$, while the starburst spectrum is ramped down during the same interval.

4 RESULTS

4.1 Physical impact

The intensity of the starburst spectrum was adjusted to ensure the hydrogen ionization front swept across the simulation volume by $z \simeq 6$, although some shadowed regions persist along the edge of the box until $z \simeq 5.5$. The intensity of the power-law spectrum was adjusted so that the HeII-ionization front swept across the box by $z \simeq 3.2$, again with some shadowing persisting to $z \lesssim 3$. This corresponds to a hydrogen ionization rate from the QSO at full intensity half that of the starburst at its full intensity.

The heating rate per ionization of HeII as the HeII ionization front passes through the box at $z = 3.3$ is shown in Fig. 2. The filtering effect of the IGM in hardening the ionizing radiation field is clearly discernible in the pre-ionized gas ahead of the ionization front. The heating rate per ionization is substantially enhanced, reaching values of up to 100–400 eV. By comparison, once the front has passed, the energy per HeII ionization is ~ 22 eV.

The resulting temperature structure is shown in Fig. 3 as the HeII I-front passes through the box at $z = 3.3$ and at $z = 2.0$, after HeII ionization has completed. The effect of shadowing produced by density inhomogeneities in the IGM are apparent as the advance of the ionization front is delayed beyond the densest regions. This may best be seen by comparing the temperature map at $z = 3.3$ in Fig. 3 with the density map in Fig. 4. (The principal density structures change little between $z = 3.3$ and $z = 2.0$ in comoving coordinates.) Large temperature boosts of $3 - 4 \times 10^4$ K occur downstream from dense clumps, consistent with the striations of high heating rates per ionization in Fig. 2 as expected for photoionization by a radiation field hardened by intervening optically thick clumps with optical depths of several tens, as discussed in Sec. 2.

By $z = 2.0$, most of the high temperature striations have been replaced by gas temperatures that trace the mat-

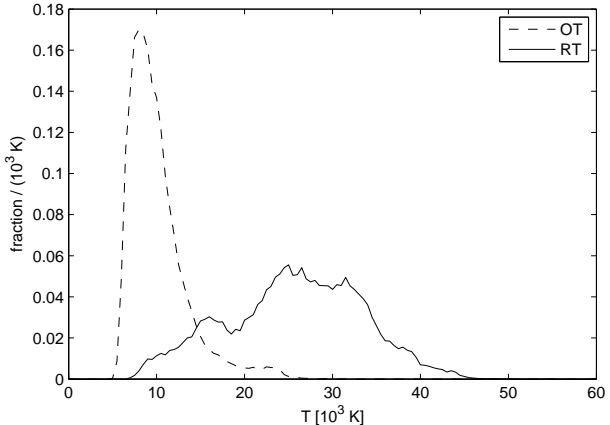


Figure 5. Distribution of temperatures at $z = 3$ following reionization including radiative transfer (solid line) vs reionization in the optically thin limit (dashed line).

ter distribution now that HeII reionization has completed. Pronounced hot regions, however, persist, particularly in underdense regions unable to achieve thermal equilibrium. These lay behind dense structures while the gas was reionized. The filtering of the radiation field by the dense structures hardened the spectrum of the incident radiation passing downstream to the underdense gas, as shown in Fig. 2, producing the high temperatures. This effect is especially prevalent in the centre-right portion of the figure.

4.2 Differential impact

Including radiative transfer in the ionization of HeII substantially boosts the temperature of the gas, increasing it typically by $15 - 20 \times 10^3$ K over the optically thin reionization limit, as shown in Fig. 5. The temperature-density relation is shown in Fig. 6. The plateau with a gas temperature of $\sim 20 - 30 \times 10^3$ K at the mean baryon density agrees well with the estimate of Schaye et al. (2000) of $T_0 \sim 20 - 30 \times 10^3$ K at $z = 3$, with only a weakly increasing temperature with overdensity, as inferred from the Doppler widths measured in high resolution spectra of the Ly α forest. The temperature found in the simulation, however, is much larger than the temperature at the mean density of $T_0 \sim 10 - 15 \times 10^3$ determined from the flux curvature method applied to high resolution data (Becker et al. 2011). The discrepancy may be due to an inadequate simulation model for calibrating the statistic used to estimate the gas temperature. Alternatively, it may indicate that either HeII was reionized too late in the simulation here, or that the HeII-ionizing source was too hard. A temperature inversion occurs for $\rho/\langle\rho\rangle > 5$, as is expected for thermal balance between photoionization heating and atomic line and radiative recombination cooling in dense structures. Only such high density gas is able to achieve thermal balance; the time scale to achieve equilibrium is too long in underdense gas (Meiksin 1994; Miralda-Escudé & Rees 1994). A similar trend between temperature and density is found for a pure dark matter simulation with radiative transfer (Tittley & Meiksin 2007).

Compared with optically thin reionization, the excess

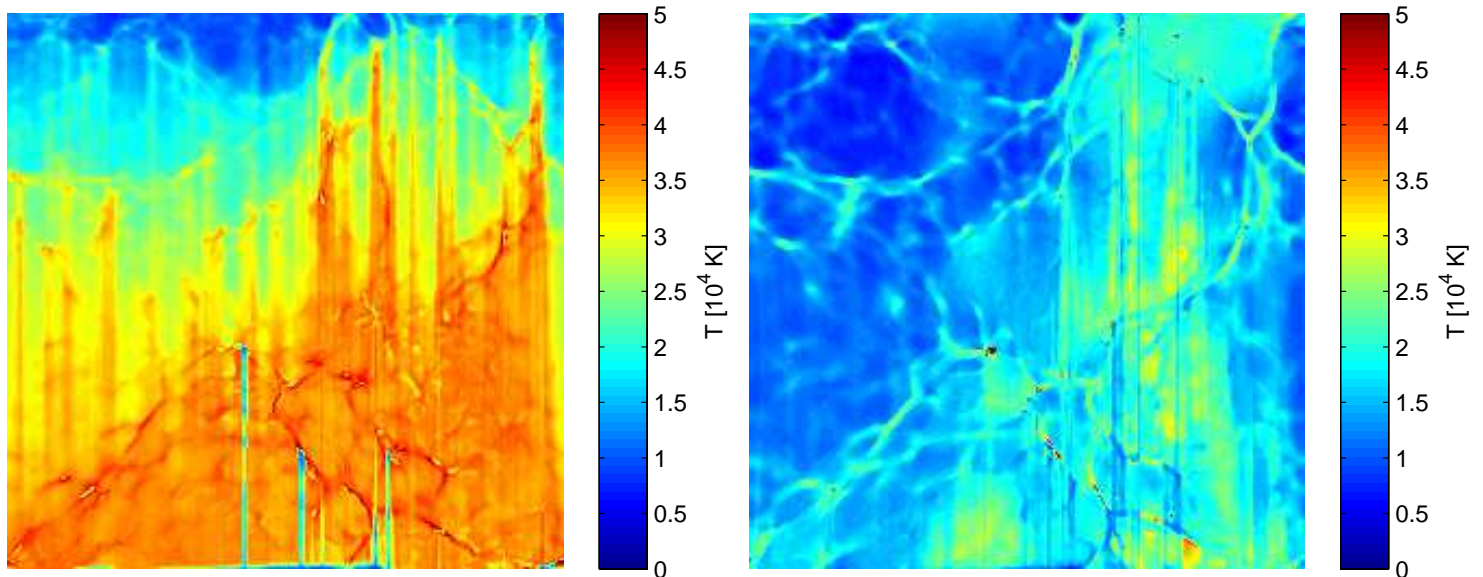


Figure 3. The post-ionization temperature for a HeII ionization front sweeping across the box from top to bottom, at $z = 3.3$ (left panel) and $z = 2.0$ (right panel). The box side is $25h^{-1}$ Mpc (comoving).

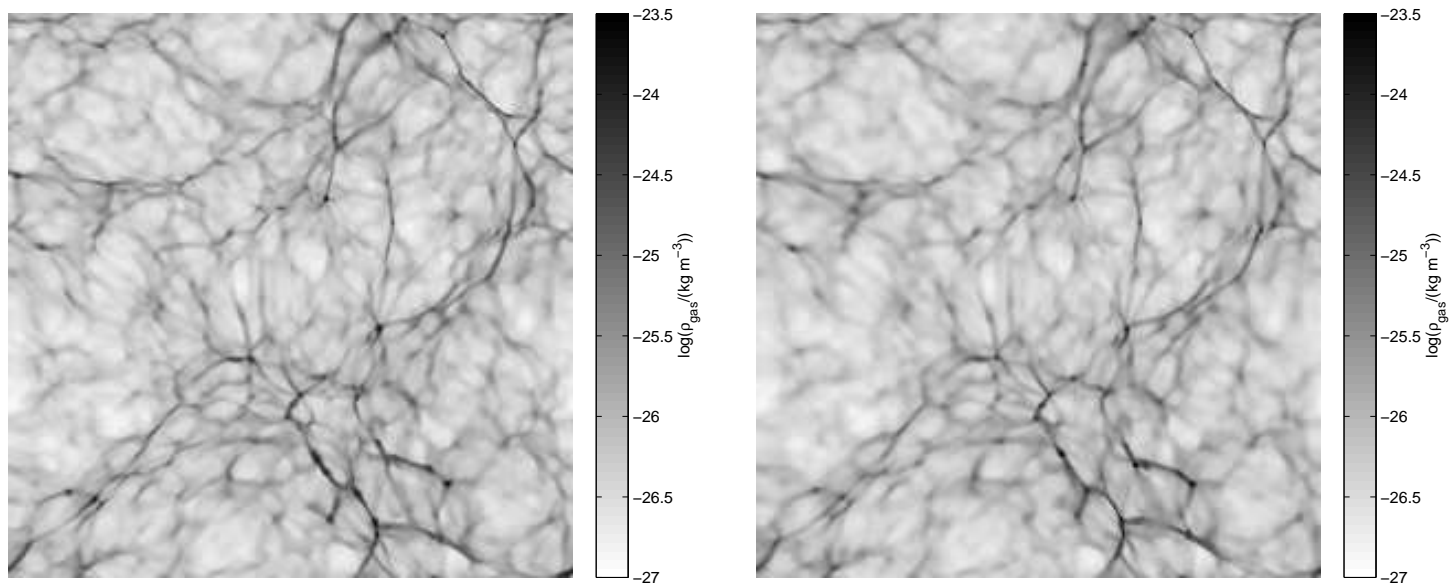


Figure 4. The gas distribution at $z = 2.0$ without HeII reionization (left panel) and with (right panel). Gas is driven out of small haloes by the HeII reionization. The box side is $25h^{-1}$ Mpc (comoving).

temperature boost allowing for radiative transfer occurs primarily for underdense gas, as shown in Fig. 6 (right panel). Most of the gas with $\rho/\langle\rho\rangle > 3$ experiences very little boost at all, as it is able to quickly recover thermal balance.

A map of the difference in the temperatures is shown in Fig. 7. Boosts of $\Delta T > 15 \times 10^3$ K are visible downstream of very dense structures which act to filter and harden the radiation field passing through them. The densest structures themselves show little change in temperature, as the temperature rapidly reaches thermal balance. Small overdense patches, however, show marked temperature deficits, as much as $\Delta T < -10 \times 10^3$ K. These regions account for the

temperature reductions in Fig. 6. The temperature decreases arise from complete shadowing of the HeII-ionizing photons by an intervening optically thick system at the HeII photoelectric edge. While for optically thin reionization, all the gas everywhere is exposed to the photoionizing background, allowing for radiative transfer will produce shadowed regions in the presence of sufficiently dense clumps of gas. Only after HeII reionization completes will the regions be reheated by overlapping ionization fronts.

The increase in the peculiar velocity compared with the computation in the optically thin approximation is shown in Fig. 8 (right panel). The differences are small, typically less

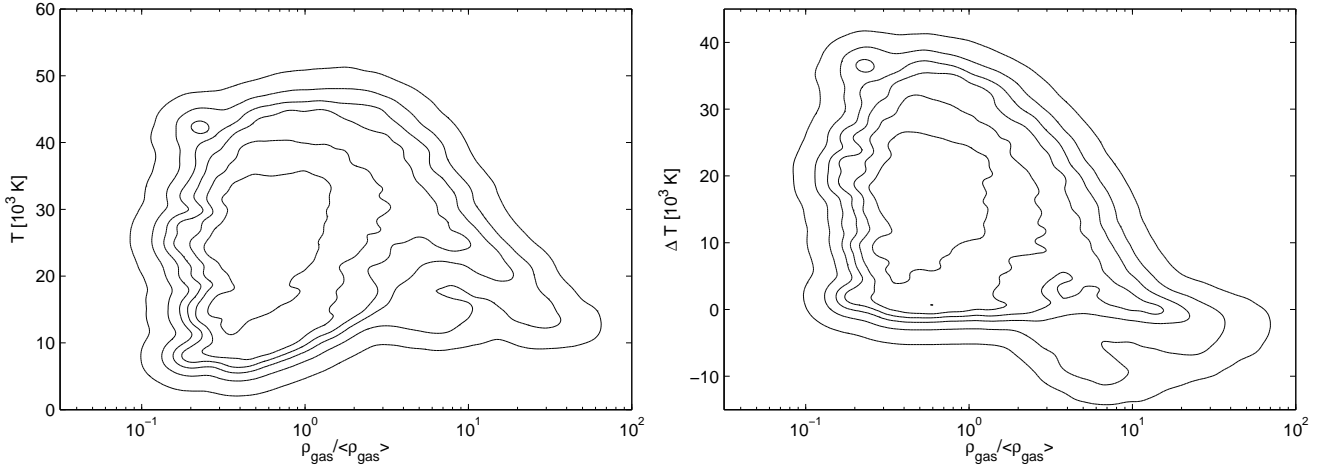


Figure 6. (Left panel) The temperature as a function of gas density at $z = 3.0$ following HeII reionization including radiative transfer. (Right panel) The boost in temperature as a function of gas density at $z = 3.0$ including radiative transfer vs reionization in the optically thin limit. The contour levels are probability density levels (per $dT-d\log_{10} \rho/(\rho)$) stepped by 0.5 dex starting at 10^{-7} .

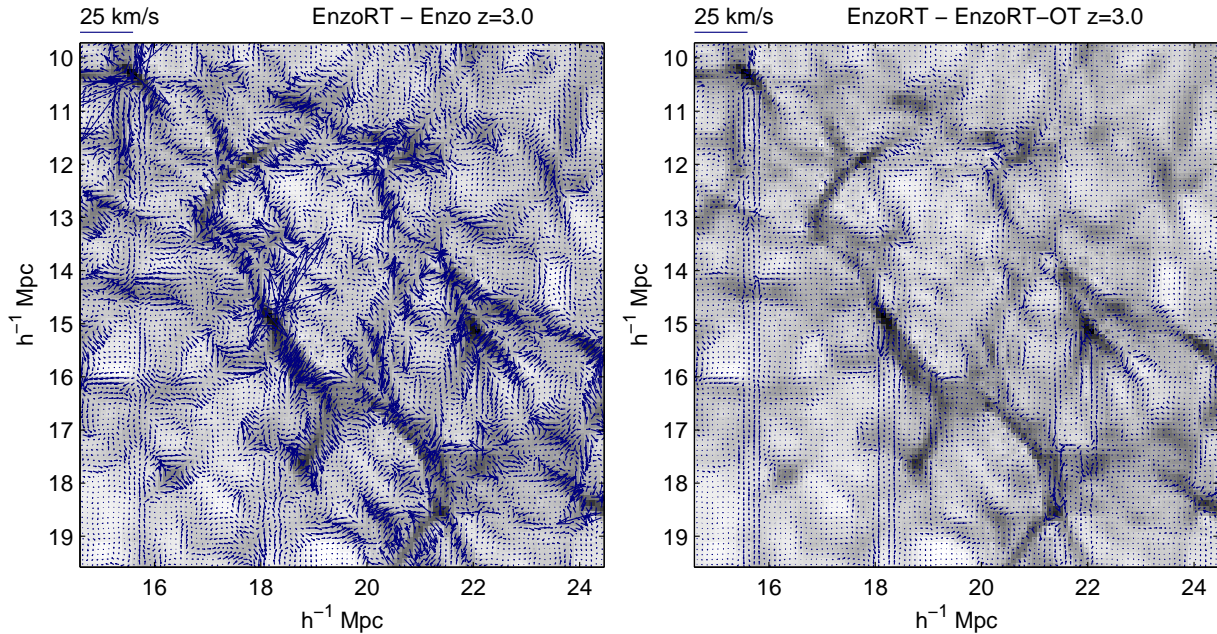


Figure 8. Differential peculiar velocity map in a kinematically complex region at $z = 3.0$. (The indicated box length scale is comoving.) Left panel: Map showing the change in the projected peculiar velocity of the gas with HeII reionization including radiative transfer from the case without HeII reionization. Right panel: Map showing the change in the projected peculiar velocity with HeII reionization including radiative transfer from the case with HeII reionization in the optically thin approximation.

than 1 km s^{-1} as shown in Fig. 9 (dashed curve), except near the most overdense structures, or behind overdense regions which shadow the incident radiation field and delay full helium reionization. The small magnitudes are in contrast to the peculiar velocity boosts induced by reionization compared with the non-reionization case, shown in the left panel. Reionization itself induces sizeable peculiar velocities, typically $0.1 < \Delta v < 10 \text{ km s}^{-1}$, throughout most of the overdense gas, as shown in Figs. 8 (left panel) and 9 (solid curve).

A comparison of the two panels in Fig. 4 shows that some of the dense gaseous clumps present in the run with-

out HeII reionization disperse when HeII reionization is included, particularly in the complex filamentary regions in the lower half of the figure. The corresponding boosts in the outflows following HeII reionization are shown in the left panel of Fig. 8. The differential impact of HeII reionization on the gas density of the IGM is shown in Fig. 10 (left panel). Substantial changes are found, with a ~ 30 per cent. decrease in underdense regions as the increased pressure gradients resulting from the additional heat input drives gas out of the shallower potential wells. Enhancements are produced as well, with the density increasing by as much as 50 per cent. in dense regions when helium reionization is

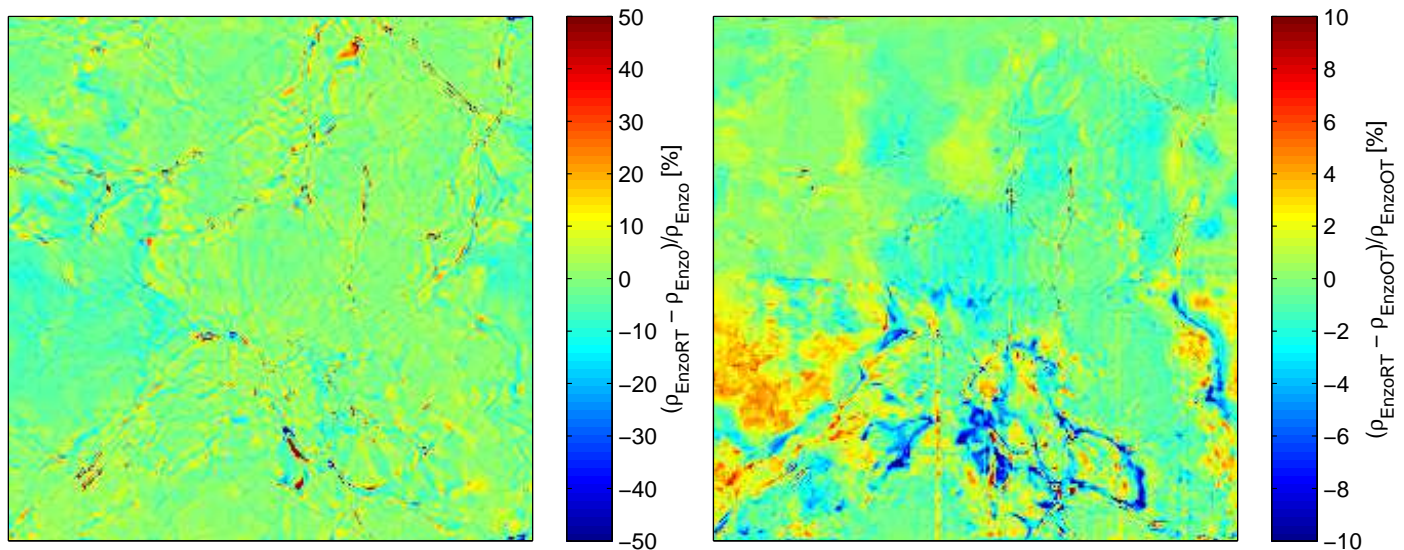


Figure 10. Maps showing the differential effect of HeII reionization on the gas density at $z = 3$. Left panel: Map showing the percentage change in the gas density with HeII reionization including radiative transfer from the case without HeII reionization. Right panel: Map showing the percentage change in the gas density with HeII reionization including radiative transfer from the case with HeII reionization in the optically thin approximation. (Note change in scale.) The box side is $25h^{-1}$ Mpc (comoving).

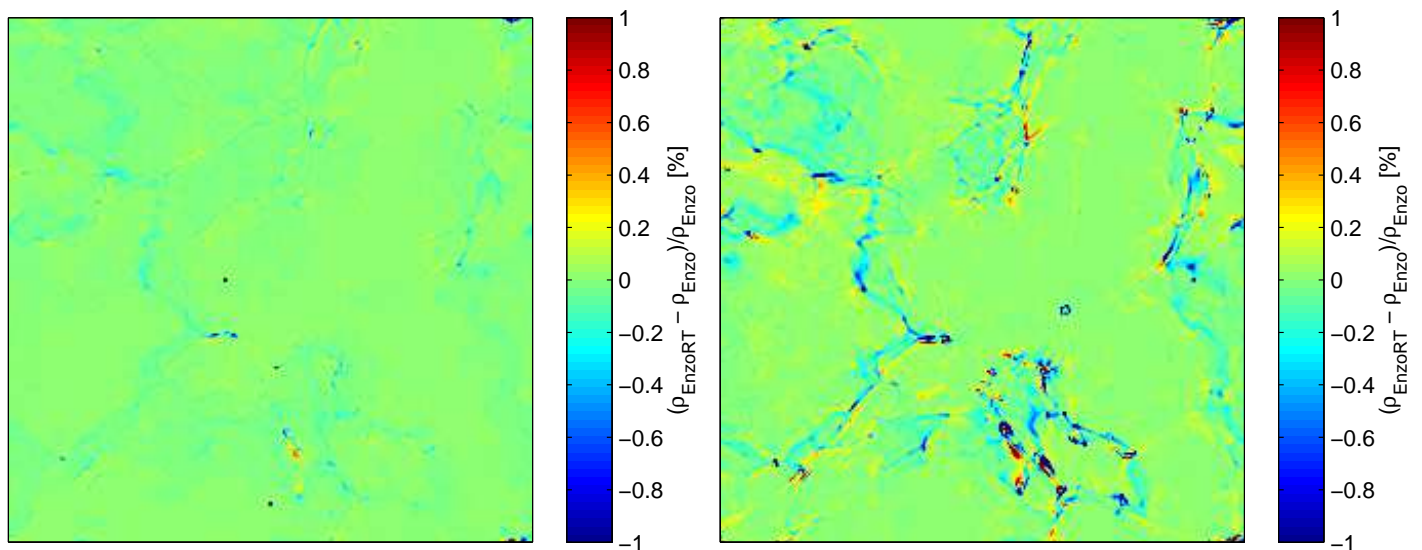


Figure 11. Maps showing the differential effect of HeII reionization on the dark matter density at $z = 3$ (left panel) and $z = 2$ (right panel). The box side is $25h^{-1}$ Mpc (comoving).

included. These regions tend to trace the filamentary structure of the gas distribution, suggesting they are too hot to accrete as readily on to nearby haloes.

Allowing for HeII reionization, but in the optically thin limit, produces a similar gas density field to that with radiative transfer, as shown in Fig. 10 (right panel). Large differences, however, occur in the more complex density regions, with the radiative transfer case generally resulting in more completely evacuated underdense regions.

The gas motion following HeII reionization also produces a change in the dark matter distribution, although at a much smaller level. As gas is driven out of filamentary

structures, the reduced gravitational potential will result in the dark matter readjusting to a somewhat lower density, as shown in Fig. 11. The differences are small at $z = 3$, on the order of 1 percent or less. By $z = 2$, however, the differences have grown to as high as 3 percent., with coherent structures several comoving megaparsecs in scale showing underdensities. As shown in Fig. 12, most of the differences are accounted for in the optically thin limit, but not entirely, especially in complex density regions such as in the lower middle region of the figure. Large-scale simulations with multiple QSO sources are necessary to estimate the impact on the matter power spectrum $P(k)$, however the

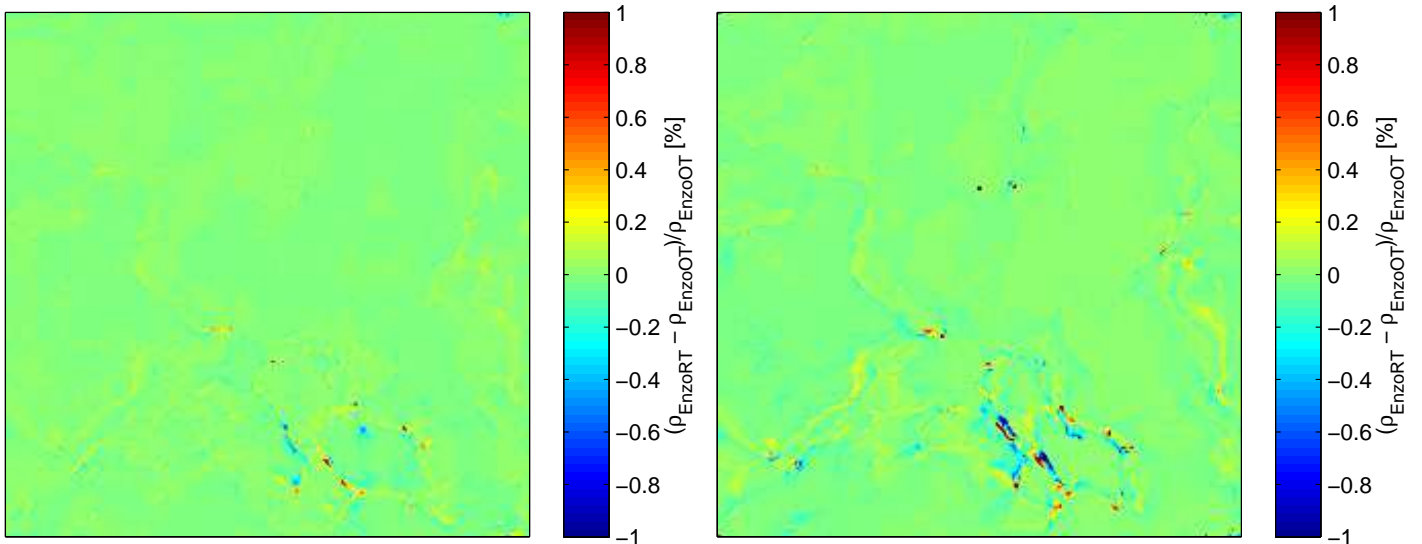


Figure 12. Maps showing the differential effect of HeII reionization on the dark matter density allowing for full radiative transfer compared with HeII reionization in the optically thin approximation. Shown at $z = 3$ (left panel) and $z = 2$ (right panel). The box side is $25h^{-1}$ Mpc (comoving).

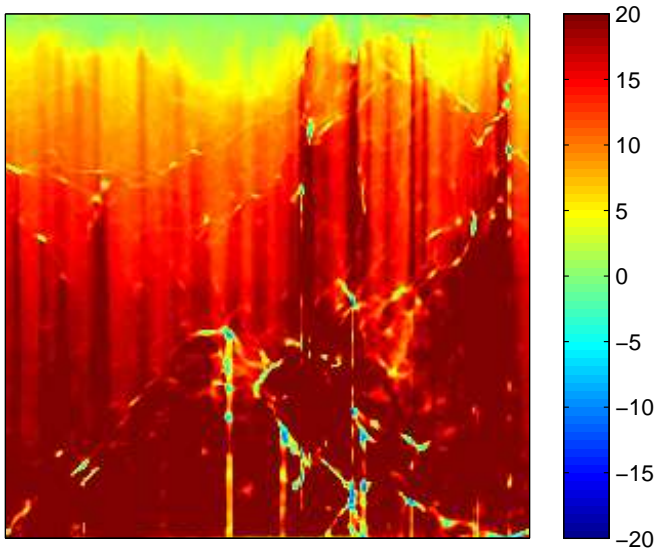


Figure 7. Map showing the change in the temperature including radiative transfer and without, at $z = 3.0$, following HeII reionization. The box side is $25h^{-1}$ Mpc (comoving).

results here suggest reionization may perturb $P(k)$ by a few per cent. on comoving scales $k > 0.5 h\text{Mpc}^{-1}$ by $z = 2$.

5 SPECTRAL SIGNATURES

To assess the impact of radiative transfer on the spectral signatures of the Ly α forest, spectra against a fictitious background source are drawn from the **Enzo** simulations with and without radiative transfer. The spectra are generated following the procedure described in Tittley & Meiksin (2007). They are constructed at an angle relative to the simulation axes in order to create a long non-repeating spectrum

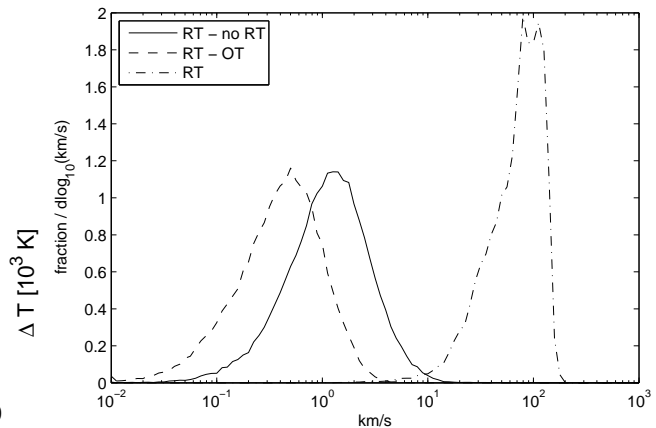


Figure 9. Distribution of peculiar velocity difference at $z = 3$ for reionization including radiative transfer vs the case with no reionization (solid line) and reionization in the optically thin limit (dashed line). Also shown is the total peculiar velocity distribution for the reionization simulation including radiative transfer (dot-dashed line).

Table 1. Effective IGM optical depths for H I and HeII Ly α .

Component	2.0	2.5	3.0	3.5	4.0
$\tau_{\text{eff}}^{\text{HI}}$	0.13	0.23	0.40	0.72	0.89
$\tau_{\text{eff}}^{\text{HeII}}$	0.45	2.0	5.0

that wraps around a slice through the simulation volume. The velocity pixel widths are 5 km s^{-1} . Both H I Ly α and HeII Ly α spectra are made. The spectra are normalised to a mean transmission of $\langle \exp(-\tau) \rangle = \exp(-\tau_{\text{eff}})$ with the

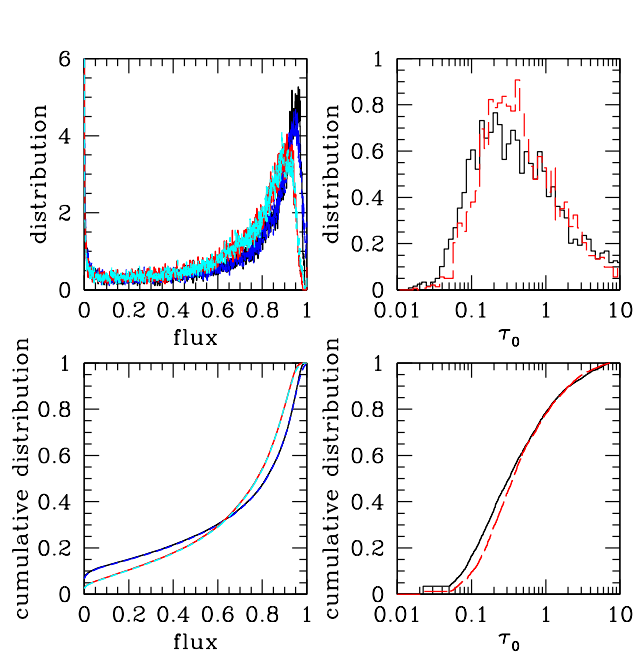


Figure 13. (Top left panel) The pixel flux distribution function at $z = 3$ following HeII reionization for **Enzo** with radiative transfer (black solid line) and in the optically thin limit (red solid line). Also shown is the recovery of the flux distribution using only the fit absorption features for the run with radiative transfer (blue short-dashed line) and without (cyan short-dashed line). (Bottom left panel) The corresponding cumulative flux distribution. (Top right panel) The distribution of line centre optical depths for the fit lines for reionization including radiative transfer (black solid line) and without (red long-dashed line). (Bottom right panel) The corresponding cumulative distribution.

values given in Table 1 for H I (Faucher-Giguère et al. 2008) and He II (Zheng et al. 2004; Shull et al. 2010). Absorption lines are fit to the spectra using **AUTOVP** (Davé et al. 1997), modified to recover from fatal errors (Meiksin et al. 2001). At $z = 3.0$, the He II Ly α transmission is very patchy and found too small to readily fit absorption line features.

5.1 H I absorption signature

The pixel flux distribution at $z = 3.0$ is shown following HeII reionization both with and without radiative transfer in Fig. 13 (left panels). Allowing for radiative transfer produces a smaller fraction of low optical depth pixels ($0.1 < \tau < 0.6$), and a larger fraction of very low values ($\tau < 0.1$), compared with the optically thin approximation (right panels).

Also shown are the flux distributions recovered by fitting absorption lines to the spectra, and regenerating the flux distribution from the absorption lines alone. These are found to accurately recover the original flux distribution, demonstrating the absence of residual absorption that may not be accounted for by absorption lines.

The distribution of line centre optical depths is provided in the right panels of Fig. 13, showing a higher fraction of lines with line centre optical depth $\tau_0 < 0.1$ for the case with radiative transfer compared with the optically thin limit. The higher proportion of very low fluctuations when radiative

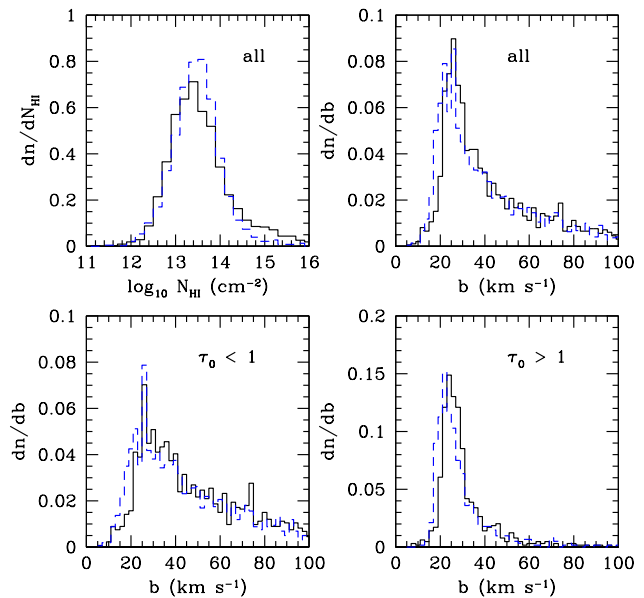


Figure 14. (Top left panel) The H I column density distribution at $z = 3$ following HeII reionization for **Enzo** with radiative transfer (solid line; black) and in the optically thin limit (dashed line; blue). (Top right panel) The corresponding Doppler parameter distribution. (Lower left panel) The Doppler parameter distribution for absorption lines with line centre optical depth $\tau_0 < 1$. (Lower right panel) The Doppler parameter distribution for absorption lines with $\tau_0 > 1$.

transfer is included may appear counter-intuitive since the temperatures, and so thermal pressures, are greater. The increased Jeans length may have been expected to smooth away small fluctuations in the spectra. Consideration of the dependence of the optical depth on the thermal width provides an explanation. Since the line centre optical depth varies as $\tau_0 \propto N_{\text{HI}}/b$, for a given column density, an increased Doppler parameter due to heating the gas to a higher temperature reduces the line centre optical depth. The increase in temperature will also decrease the recombination rate at a given gas density, and so reduce the H I column density.

The column density and Doppler parameter distributions for the absorption line fits to the spectra are shown in Fig. 14. The column density distributions for the simulations with and without radiative transfer are very similar, with the distribution for the RT case somewhat broader. By contrast, the Doppler parameter distribution for the RT case shows a higher cutoff at the low end compared with the optically thin case. Dividing the lines into those optically thin and optically thick at line centre reveals that a large contribution to the offset originates from the optically thin lines. The median Doppler parameter of the optically thin absorption lines for the RT case is $b_{\text{med}} \simeq 45 \text{ km s}^{-1}$, while for the optically thin case, $b_{\text{med}} \simeq 41 \text{ km s}^{-1}$. For the optically thick absorbers, $b_{\text{med}} \simeq 26 \text{ km s}^{-1}$ for the RT case, while for the optically thin reionization case $b_{\text{med}} \simeq 24 \text{ km s}^{-1}$. Since the optically thin absorbers arise in moderate to low overdensity structures, the gas in the optically thin systems is too rarefied to establish thermal balance between radiative

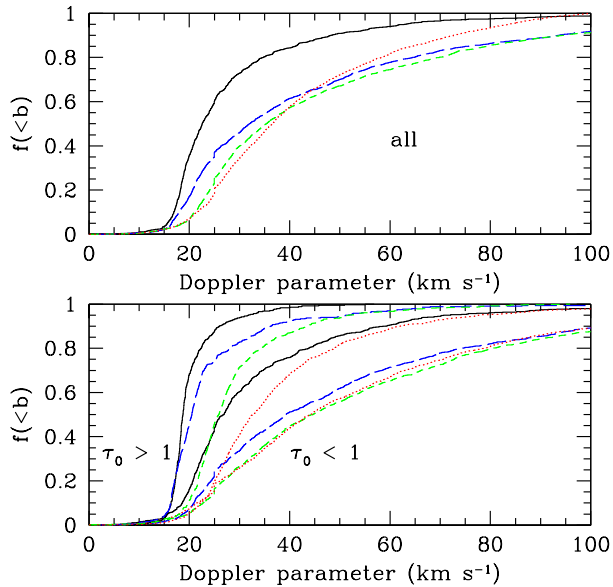


Figure 15. (Top panel) The H I Doppler parameter cumulative distribution for *Enzo* with radiative transfer, shown at $z = 2$ (solid line; black), 2.5 (long-dashed line; blue), 3.0 (short-dashed line; green) and 3.5 (dotted line; red). (Bottom panel) As in the top panel, but with the lines divided between those with line centre optical depth $\tau_0 < 1$ (rightmost curves) and those with $\tau_0 > 1$ (leftmost curves).

heating and atomic cooling. As a consequence, the systems are overheated (Miralda-Escudé & Rees 1994; Meiksin 1994; Meiksin et al. 2001).

A similar trend was found for the optically thin reionization models of Meiksin et al. (2001) compared with the data: the median Doppler parameter of the measured optically thin lines were broader than the lines drawn from the best-fitting Λ CDM model simulation. The median Doppler parameter for lines with $\tau_0 < 1$ measured in the spectrum of Q1937–1009 (Burles & Tytler 1997), over the redshift range $3.1 < z < 3.7$ was found to be $b_{\text{med}} \simeq 29 \text{ km s}^{-1}$, while the best-fitting model gave $b_{\text{med}} \simeq 20 \text{ km s}^{-1}$. The measured median value for the systems with $\tau_0 < 1$ is substantially smaller than found here for the RT simulation, suggesting the He II reionization was too recent in the simulation (cf. Tittley & Meiksin (2007); Meiksin et al. (2010)), or that the input spectrum too hard on average. By contrast, the data for the $\tau_0 > 1$ systems gave $b_{\text{med}} \simeq 26 \text{ km s}^{-1}$, in agreement with the RT simulation result found here. A fully fair comparison with the observations, however, would require replicating the redshift range, resolution and noise properties of the measured spectra, as well as varying the luminosities, spectral shapes and timings of the sources. Such a comparison would require a large suite of simulations, which is not the purpose of this paper.

The evolution of the Doppler parameter cumulative distribution is shown in Fig. 15. The distributions show little evolution over $2.5 < z < 3.5$, but a marked decrease in the Doppler parameters by $z = 2.0$ as the IGM adiabatically cools following He II reionization. Dividing the absorp-

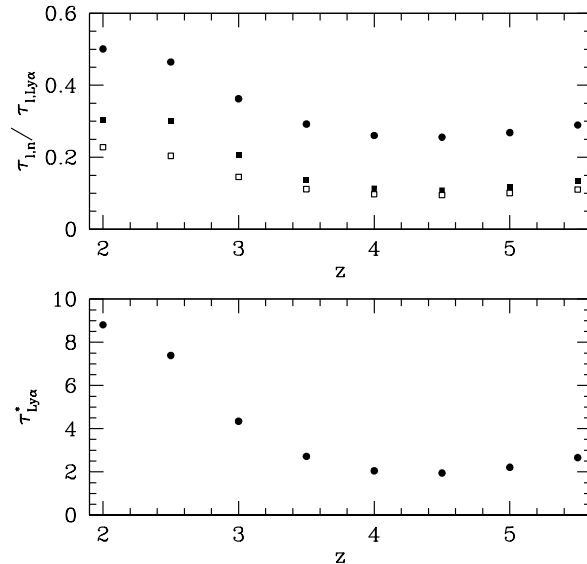


Figure 16. (Top panel) The ratios of the effective optical depths $\tau_{l,\text{Ly}\beta}/\tau_{l,\text{Ly}\alpha}$ (solid points) and $\tau_{l,\text{Ly}\gamma}/\tau_{l,\text{Ly}\alpha}$ (solid squares) for H I obtained from the *Enzo* simulation with radiative transfer, as a function of redshift z . Also shown is the predicted ratio $\tau_{l,\text{Ly}\gamma}/\tau_{l,\text{Ly}\alpha}$ (open squares) based on a line-blanketing model (see text). (Bottom panel) The characteristic H I $\tau_{\text{Ly}\alpha}^*$ optical depth inferred from the values of $\tau_{l,\text{Ly}\beta}/\tau_{l,\text{Ly}\alpha}$ from the *Enzo* simulation with radiative transfer.

tion lines into those optically thick and thin at line centre (bottom panel), reveals that the optically thick systems undergo continual evolution towards smaller values with cosmic time, with the median Doppler parameter evolving from $b_{\text{med}} \simeq 33 \text{ km s}^{-1}$ at $z = 3.5$ to 19 km s^{-1} by $z = 2.0$ as the gas establishes thermal balance following He II reionization. By contrast, the systems optically thin at line centre show almost no evolution between $z = 3.5$ and 3.0, with heavily broadened lines following He II reionization having a median Doppler parameter $b_{\text{med}} \simeq 44 \text{ km s}^{-1}$, diminishing slightly to 39 km s^{-1} at $z = 2.5$, and then substantially to 27 km s^{-1} by $z = 2.0$.

In addition to the scattering of Ly α photons, the higher order Lyman resonance line photons will be scattered as well. Identifying individual absorption features in spectra is difficult except for the strongest lines, especially at high redshifts. The effective optical depths resulting from line blanketing, however, may be inferred. The observed effective optical depth at redshift z due to systems with restframe equivalent widths w (in wavelength units) is given by

$$\tau_{l,\text{Ly}n} = \frac{1+z}{\lambda_{1n}} \int dw \frac{\partial^2 N}{\partial z \partial w} w, \quad (10)$$

where λ_{1n} is the wavelength of the Lyman resonance line transition to the n^{th} principal quantum level, and where the equivalent width is related to the line centre optical depth $\tau_{0,1n}$ by $w = 2(b/c)\lambda_{1n}F(\tau_{0,1n})$, where $F(\tau)$ is a function dependent on the Voigt profile (Meiksin 2009). If the line distribution is separable into the form $\partial^2 N / \partial z \partial w = (dN/dz)f(w/w_{1n}^*)$, where the equivalent width distribution

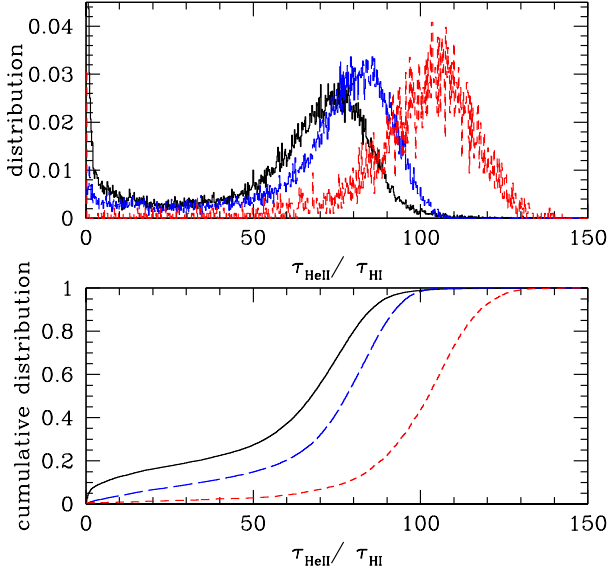


Figure 17. (Top panel) The distributions of the ratio of the pixel optical depths $\tau_{\text{HeII}}/\tau_{\text{HI}}$ in the spectra following HeII reionization for Enzo with radiative transfer at $z = 2.0$ (solid line; black), 2.5 (long-dashed line; blue) and 3.0 (short-dashed line; red). (Bottom panel) The corresponding cumulative distributions.

$f(w/w_{1n}^*)$ may be characterised by a single parameter w_{1n}^* , such as the scale height for an exponential distribution $f(w/w_{1n}^*) = \exp(-w/w_{1n}^*)$, then the optical depths for transitions to levels n and n' are related by

$$\frac{\tau_{l,n'}}{\tau_{l,n}} = \frac{F\left(\frac{\lambda_{1n'} f_{1n'}}{\lambda_{1n} f_{1n}} \tau_{0,1n}^*\right)}{F(\tau_{0,1n}^*)}, \quad (11)$$

where $\tau_{0,1n}^*$ is given by $w_{1n}^* = 2(b/c)\lambda_{1n}F(\tau_{0,1n}^*)$.

The ratios $\tau_{l,\text{Ly}\beta}/\tau_{l,\text{Ly}\alpha}$ and $\tau_{l,\text{Ly}\gamma}/\tau_{l,\text{Ly}\alpha}$ from the Enzo simulation with RT are shown in the upper panel of Fig. 16. A rise in both ratios occurs at redshifts $z < 4$ once HeII reionization begins. The inferred values of the characteristic Ly α optical depth $\tau_{\text{Ly}\alpha}^*$ are shown in the bottom panel. The corresponding predicted values of $\tau_{l,\text{Ly}\gamma}/\tau_{l,\text{Ly}\alpha}$ (upper panel) lie close to, but somewhat below, the values measured from the simulation, suggesting the single parameter separable model for the line distribution provides a good description of the line blanketing, but becomes less accurate at large values of $\tau_{\text{Ly}\alpha}^*$.

5.2 HeII absorption signature

For a homogeneous radiation field, the ratio of the HeII to H I optical depths per pixel is

$$\frac{\tau_{\text{HeII}}}{\tau_{\text{HI}}} = \frac{1}{4} \frac{N_{\text{HeII}}}{N_{\text{HI}}} \frac{b_{\text{HI}}}{b_{\text{HeII}}}, \quad (12)$$

where N_{HI} and N_{HeII} are the H I and HeII column densities, respectively, and b_{HI} and b_{HeII} the corresponding Doppler parameters. For pure thermal broadening, $b_{\text{HeII}} = b_{\text{HI}}/2$, while for velocity-broadened lines, $b_{\text{HeII}} = b_{\text{HI}}$. For metagalactic H I and HeII photoionization rates Γ_{HI} and Γ_{HeII} ,

the column density ratio, for a hydrogen to helium number density ratio of 12.9, is

$$\begin{aligned} \frac{N_{\text{HeII}}}{N_{\text{HI}}} &= \frac{\Gamma_{\text{HI}}}{\Gamma_{\text{HeII}}} \frac{n_{\text{He}}}{n_{\text{H}}} \frac{\alpha_{\text{HeIII}}}{\alpha_{\text{HI}}} \\ &\simeq 0.31 \frac{\Gamma_{\text{HI}}}{\Gamma_{\text{HeII}}} \frac{7.107 - (1/2) \log T + 0.00547T^{1/3}}{6.414 - (1/2) \log T + 0.00868T^{1/3}} \\ &\simeq 0.42 \frac{\Gamma_{\text{HI}}}{\Gamma_{\text{HeII}}}, \end{aligned} \quad (13)$$

where the last form is accurate to 5 per cent. for $10^4 < T < 5 \times 10^4$ K (Madau & Meiksin 1994; Meiksin 2009). The optical depth ratio is thus a measure of the fluctuations in the ratio of the radiation field as well as the velocity-broadening of the absorption lines.

The distribution of the optical depth ratio per pixel is shown in Fig. 17 for $2 < z < 3$. The distributions show a wide range of values, with the peak declining from 105 at $z = 3$ to 75 at $z = 2$. The FWHM of the distributions is about 30, changing little with redshift. The variations arise entirely from the radiative transfer of the incident radiation through an inhomogeneous medium following helium reionization. Allowing for the Poisson fluctuations from the finite number of sources within an attenuation volume for HeII-ionizing photons will further enhance the fluctuations (Fardal et al. 1998; Bolton et al. 2006; Meiksin 2009; Furlanetto & Dixon 2010).

Absorption lines were fit in the HeII spectrum at $z = 2.5$, and matched to the H I features, requiring a line-centre velocity difference smaller than 10 km s^{-1} for a successful match. The relation between the matching line centre optical depths is shown in Fig. 18. While the deblending of absorption features will introduce scatter into the relation, a clear correlation is apparent in the upper left panel corresponding to $\tau_{0,\text{HeII}}/\tau_{0,\text{HI}} \lesssim 100$. The ratio is found to decrease towards increasing $\tau_{0,\text{HI}}$ (lower left panel). This arises as the H I features become saturated. A similar trend was found for simulated spectra by Fechner et al. (2006) for absorption lines in the redshift range $2.30 \lesssim z \lesssim 2.75$, who argued statistical comparisons must be restricted to systems with $\tau_{0,\text{HI}} < 0.1$.

The distribution of column density ratios $\eta = N_{\text{HeII}}/N_{\text{HI}}$ in Fig. 18 shows a similar decreasing trend towards increasing N_{HI} (top right panel). A broad distribution of η values for all the systems is found (lower right panel). Restricting the systems to those with $0.01 < \tau_{0,\text{HI}} < 0.1$, however, results in a far sharper distribution centred at $\eta \simeq 130$. The distributions are very similar to those measured (Fechner et al. 2006), with the distribution for systems restricted to $0.01 < \tau_{0,\text{HI}} < 0.1$ peaking at $\eta \lesssim 100$ and somewhat broader than the distribution found from the Enzo RT simulation. The peak in the distribution from the simulation is fixed by the normalisations imposed on the effective H I and HeII optical depths. The agreement in the widths of the distribution, however, is a product of radiative transfer within the simulation. While the measured mean and breadth of the distribution may be reproduced by the QSO luminosity function, taking into account the Poisson fluctuations in QSO numbers within a HeII-ionizing photon attenuation volume in a homogeneous IGM (Meiksin 2009), the results found here demonstrate that a large contribution to the breadth in the distribution is expected to arise from variations in the HeII ionizing background resulting from

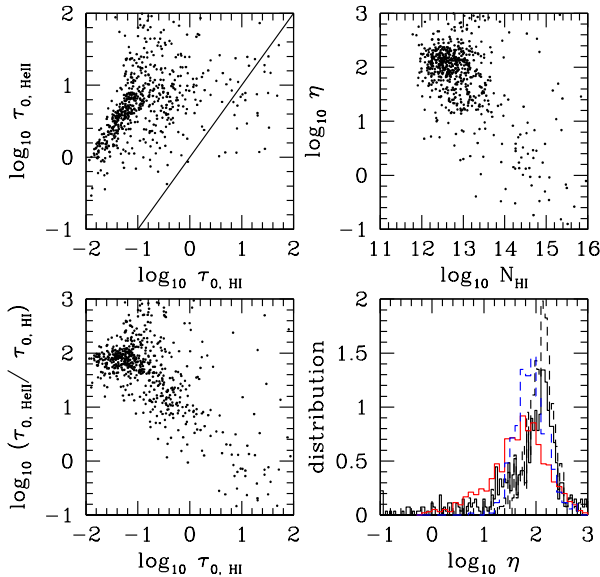


Figure 18. Comparison of *Enzo* RT simulation results for H I and He II line centre optical depths and column densities for fit absorption features at $z = 2.5$. (Top left panel) Comparison of line centre optical depths for H I and He II absorption features. The solid line shows the relation $\tau_{0,\text{HeII}} = \tau_{0,\text{HI}}$. (Bottom left panel) He II to H I line centre optical depth ratio vs H I line centre optical depth. (Top right panel) He II to H I column density ratio η vs H I column density. (Bottom right panel) Distribution functions of η for all lines (solid black histogram), and lines restricted to $0.01 < \tau_{0,\text{HI}} < 0.1$ (dashed black histogram). Also shown are the distribution functions for HS 1700+6416 (Fechner et al. 2006) for absorption features in the redshift range $2.30 \lesssim z \lesssim 2.75$ for all the lines (solid red histogram) and for lines restricted to $0.01 < \tau_{0,\text{HI}} < 0.1$ (blue dashed histogram). All distribution functions are normalised to unit area.

the effect of inhomogeneities in the density field of the IGM on the radiation transfer of the impinging radiation field.

The peak and FWHM in the distribution of η at $z = 2.5$ from the simulation correspond to an effective $\Psi = \Gamma_{\text{HI}}/\Gamma_{\text{HeII}} \simeq 300^{+150}_{-100}$. For a metagalactic spectral shape $f_\nu \sim \nu^{-\alpha_{\text{MG}}}$, the ratio would be $\Gamma_{\text{HI}}/\Gamma_{\text{HeII}} \sim 4^{1+\alpha_{\text{MG}}}$. The match to the effective Ψ corresponds to effective spectral indices of $2.9 < \alpha_{\text{MG}} < 3.5$, much larger than the assumed source spectral index 0.5. The ratio corresponds to the expected softening of the incident spectrum due to radiative transfer through the IGM (Madau & Meiksin 1994; Haardt & Madau 1996). The required rescaling of Ψ imposed on the simulations to match the measured effective H I and He II optical depths corresponds to a pre-rescaled ambient radiation field with an average $\alpha_{\text{MG}} \simeq -0.25$ between the H I and He II Lyman edges arising exclusively from the radiative transfer of the input source spectrum through the simulation volume. This corresponds to the hardening effect of the IGM on the input radiation field. The modification of Ψ within the simulation produced by radiative transfer is found to be highly inhomogeneous, with typically 40–60 per cent. variations produced in the He II ionization rate during the passage of the He III ionization front. The larger val-

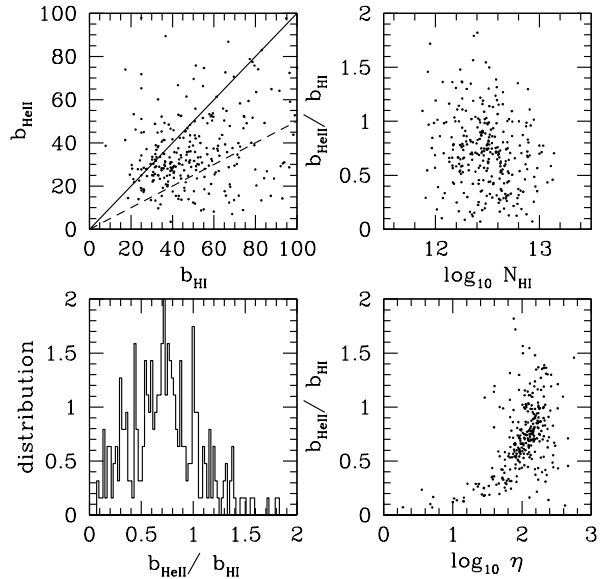


Figure 19. Comparison of *Enzo* RT simulation results for H I and He II Doppler parameters for fit absorption features at $z = 2.5$ with $0.01 < \tau_{0,\text{HI}} < 0.1$. (Top left panel) Comparison of b_{HI} and b_{HeII} absorption features. The solid line shows the relation for pure velocity broadening; the dashed line shows the relation for pure thermal broadening. (Bottom left panel) The distribution function of $b_{\text{HeII}}/b_{\text{HI}}$. (Top right panel) Doppler parameter ratio vs H I column density. (Bottom right panel) Doppler parameter ratio vs He II to H I column density ratio η .

ues of Ψ are comparable to those inferred from observations (Zheng et al. 2004; Reimers et al. 2005; Fechner et al. 2006; Shull et al. 2010).

The relation between the H I and He II Doppler parameters for the absorption systems at $z = 2.5$ is shown in Fig. 19. The H I absorption lines are restricted to those with $0.01 < \tau_{0,\text{HI}} < 0.1$. In the limit of pure thermal broadening, the He II to H I ion mass ratio would result in He II systems with $\xi = b_{\text{HeII}}/b_{\text{HI}} = 1/2$. In the limit of velocity broadened lines, $\xi = 1$. The upper left panels show that the Doppler parameters lie predominantly between these two limiting cases, a consequence of fitting lines to blended features as well as to saturated He II features. The wide scatter suggests the Doppler parameter ratio ξ is not a precise indicator of the relative contributions to line broadening due to thermal motions and internal flows. Similar results were found for selected unblended absorption systems in the spectrum of HE 2347–4342 in the redshift range $2.7 < z < 2.8$, although the ratios tended more towards velocity broadening than thermal (Zheng et al. 2004). No strong correlation is found between ξ and N_{HI} (top right panel), however the ratio tends to increase with increasing η (bottom right panel), although this may be an effect of line deblending.

The ratios $\tau_{l,\text{Ly}\beta}/\tau_{l,\text{Ly}\alpha}$ and $\tau_{l,\text{Ly}\gamma}/\tau_{l,\text{Ly}\alpha}$ for He II from the *Enzo* simulation after reionization completes at $z \leq 3$ are shown in the upper panel of Fig. 20, renormalizing the spectra by $\tau_{l,\text{Ly}\alpha}$ to the values indicated. In the region of overlap, these values agree with the simulation results quoted

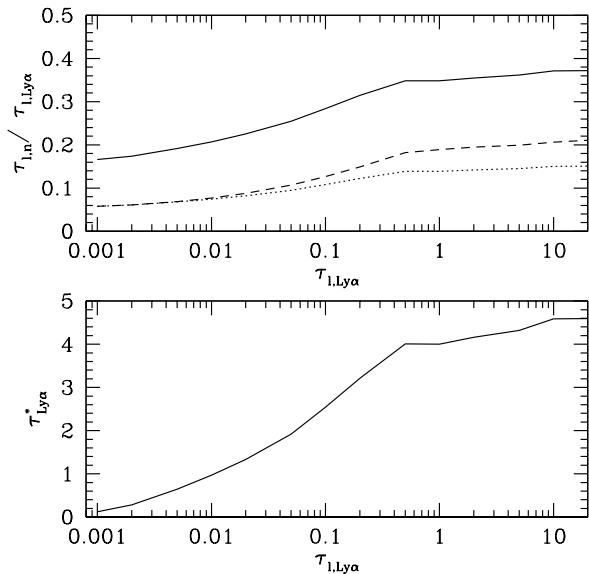


Figure 20. (Top panel) The ratios of the effective optical depths $\tau_{l,Ly\beta}/\tau_{l,Ly\alpha}$ (solid line) and $\tau_{l,Ly\gamma}/\tau_{l,Ly\alpha}$ (dashed line) for HeII obtained from the *Enzo* simulation with radiative transfer, as a function of $\tau_{l,Ly\alpha}$. (The result is insensitive to redshift after reionization completes at $z \leq 3$.) Also shown is the predicted ratio $\tau_{l,Ly\gamma}/\tau_{l,Ly\alpha}$ (dotted line) based on a line-blanketing model (see text). (Bottom panel) The characteristic HeII $\tau_{Ly\alpha}^*$ optical depth inferred from the values of $\tau_{l,Ly\beta}/\tau_{l,Ly\alpha}$ from the *Enzo* simulation with radiative transfer.

in Syphers et al. (2011). The inferred effective line centre optical depths $\tau_{0,Ly\alpha}^*$ using Eq.(11) are shown in the lower panel. The resulting predicted values for $\tau_{l,Ly\gamma}/\tau_{l,Ly\alpha}$ from Eq.(11) are shown by the dotted line in the upper panel. The values agree well with those measured directly from the simulation, indicating the absorption is well described by the line model, although the small deviation for large optical depths suggests the simple one-parameter model only approximately describes the underlying distribution at these large optical depths.

For comparison, the value measured in the QSO HE 2347–4342 ($z_{em} \simeq 2.89$), with $\tau_{Ly\alpha}^{eff} \simeq 2.393 \pm 0.015$ at $\langle z \rangle \simeq 2.8$, is $\tau_{Ly\beta}^{eff}/\tau_{Ly\alpha}^{eff} \simeq 0.31 \pm 0.04$, using the data from Syphers et al. (2011). This agrees well with the value of $\tau_{l,Ly\beta}/\tau_{l,Ly\alpha} \simeq 0.36$ predicted from the *Enzo* simulation with radiative transfer, as shown in Fig. 20.

6 COMPARISON WITH APPROXIMATE METHODS

6.1 Approximate methods

Two approximate simulation methods have been used in the past to characterise the effects of HeII reionization on the IGM. One method uses N -body code results to represent the fluid by rescaling the dark matter density (Tittley & Meiksin 2007; McQuinn et al. 2009); it thus does not account for the hydrodynamical response of the gas to heating due to radiative transfer. A similar method

post-processes hydrodynamical simulations using a radiative transfer module, but also does not include the hydrodynamical response of the gas to the radiative transfer (Bolton & Haehnelt 2007). An alternative method artificially boosts the HeII heating rates in optically thin gravity-hydrodynamics reionization simulations to mimic the boost in temperatures resulting from radiative transfer effects (Bryan & Machacek 2000).

To estimate the importance of hydrodynamical feedback effects on the observed properties of the Ly α forest, we compare the results of the hydrodynamics simulations including radiative transfer with the results of the N -body radiative transfer code PMRT (Tittley & Meiksin 2007). PMRT assumes the baryons trace the dark matter. The code is thus not able to cope with sudden increases in the pressure forces as the gas is heated and driven out of shallow potential wells or heated by shocks in collapsing structures.

Past comparisons with full hydrodynamics computations without radiative transfer show that the method recovers the distribution of Doppler parameters to high accuracy, although the median Doppler parameter may be slightly broadened by $1-2 \text{ km s}^{-1}$ (Meiksin & White 2001). A pseudo-hydrodynamics scheme with radiative transfer has the advantages over a fully hydrodynamical one of ease of implementation and a much reduced memory requirement, permitting simulations in larger boxes at the high spatial resolution required to resolve the structures in the IGM that give rise to the full range of measurable absorption systems. Here we examine how successful PMRT simulations are at capturing the essential features of the Ly α forest predicted by full hydrodynamics computations including radiative transfer.

The PMRT runs used 512^3 gravitating particles, with the identical initial particle distributions in position and velocity as for the *Enzo* runs, and the identical cosmological parameters. It used the identical radiative transfer module as for the *Enzo* runs, using 256^3 cells to represent the fluid. Following Tittley & Meiksin (2007), all cells with fewer than 100 particles were convolved over a radius of 1.5 cells to match the gas distribution from *Enzo*.

We also implement the alternative method of artificially boosting the HeII heating rate in a hydrodynamical simulation in the optically thin limit to make up for the shortfall in the additional heating due to radiative transfer effects. A boost by a factor of 2 was found to provide sufficient heat to broaden the absorption lines close to the measured values at $z \simeq 3$ (Bryan & Machacek 2000). We recompute the reionization simulation using *Enzo* with the HeII heating rate per HeII ion boosted to $G'_{HeII} = 2G_{HeII}$, and the radiative transfer switched off.

6.2 Physical properties of IGM

Maps of the IGM temperature are shown in Fig. 21 at $z = 3.3$, shortly before HeII reionization completes, and in Fig. 22 at $z = 2$, well after completion. At $z = 3.3$, the PMRT run matches most closely to the *Enzo* with RT simulation. There are, however, some conspicuous differences. The temperature structures tend to be sharper in the PMRT simulation, as it lacks both shock heating and the pressure forces that smooth the gas. The effect of shadowing by dense clumps is also more prevalent in the PMRT simulation. This is

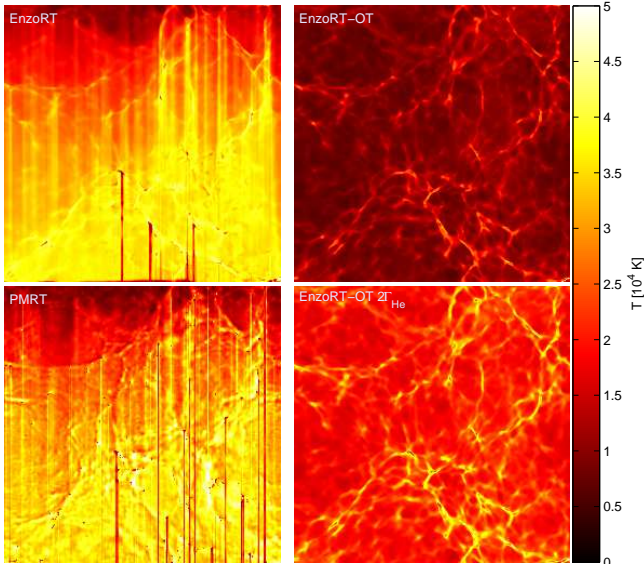


Figure 21. Temperature map at $z = 3.3$, shortly before HeII reionization completes. The ionization front sweeps across the boxes from top to bottom. The maps are shown for **Enzo** with radiative transfer (upper left), in the optically thin limit (upper right), in the optically thin limit with the HeII heating rate doubled (lower right), and for the pseudo-hydrodynamics code **PMRT** (lower left). The box side is $25h^{-1}$ Mpc (comoving).

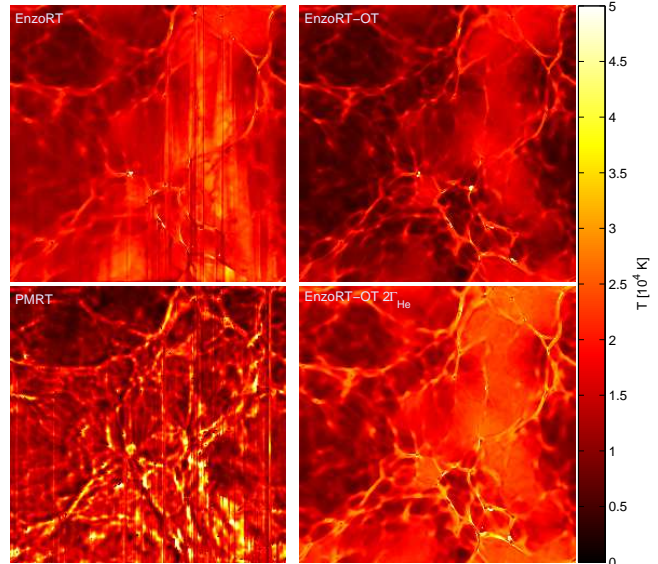


Figure 22. Temperature map at $z = 2.0$, well after HeII reionization completes. The ionization front swept across the boxes from top to bottom. The maps are shown for **Enzo** with radiative transfer (upper left), in the optically thin limit (upper right), in the optically thin limit with the HeII heating rate doubled (lower right), and for the pseudo-hydrodynamics code **PMRT** (lower left). The box side is $25h^{-1}$ Mpc (comoving).

a consequence of the inability of the dense regions to expand due to pressure forces as the ionization front sweeps across and boosts the gas temperature and pressure, as discussed in Sec. 4.2. The **Enzo** simulation with the boosted HeII heating rate recovers the high temperatures in the filaments, but the temperature in the underdense regions, although warmer than the optically thin simulation, still lies well below the **Enzo** simulation with radiative transfer.

By $z = 2.0$, the **PMRT** simulation shows significant discrepancies in the gas temperature within the filaments compared with the **Enzo** RT simulation. In contrast to the hydrodynamics simulation which accounts for the hydrodynamical response of the gas to the extra heating following HeII reionization, allowing it to expand and cool, the **PMRT** simulation keeps the gas too hot. In underdense regions, the **PMRT** simulation over-estimates the amount of adiabatic cooling, resulting in the gas becoming too cold. The **Enzo** simulation with the boosted HeII heating rate is better able to reproduce the temperatures in the underdense regions, but maintains the gas in the filaments at too high temperatures compared with the **Enzo** RT simulation.

These effects may be quantified using the temperature–density distributions extracted from the simulations. The temperature–density distribution obtained with **PMRT** closely resembles that found using **Enzo** with radiative transfer at $z \geq 3.0$, as shown in Fig. 23, with reasonably good agreement down to $z = 2$. The distributions overlap very closely, although the hydrodynamics computation shows a somewhat tighter and flatter distribution in temperatures, especially towards $z = 2$. While the temperatures in the optically thin simulation with boosted HeII heating rate agree well with the RT simulations for $\rho/\langle\rho\rangle > 3$ over $3.0 \leq z \leq 3.5$, the temperatures are appreciably lower in structures with

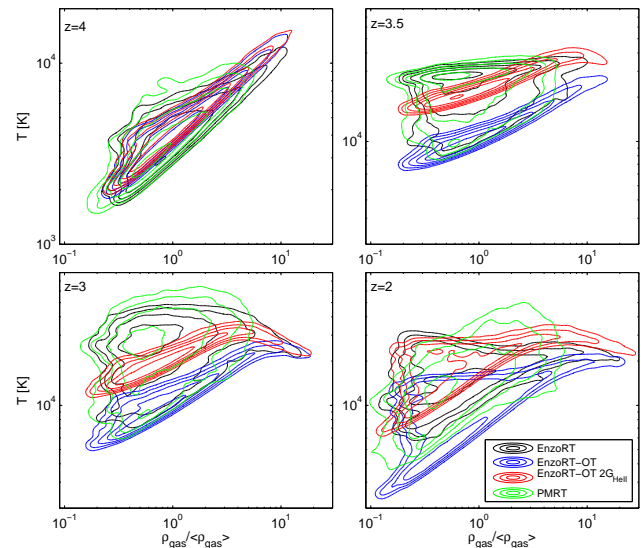


Figure 23. Temperature–density distributions at $z = 4.0, 3.5, 3.0$ and 2.0 following HeII reionization, for computation using **Enzo** with radiative transfer, **Enzo** in the optically thin limit, **Enzo** in the optically thin limit but with the HeII heating rate doubled, and the pseudo-hydrodynamics RT code **PMRT**. Note the smaller temperature scale at $z = 4.0$, prior to HeII reionization. The distributions are normalised to unity. The contour levels are at probability density levels (per $d \log_{10} T-d \log_{10} \rho/\langle\rho\rangle$) 0.1, 0.32, 1.0, 3.2, 10, 32, ...

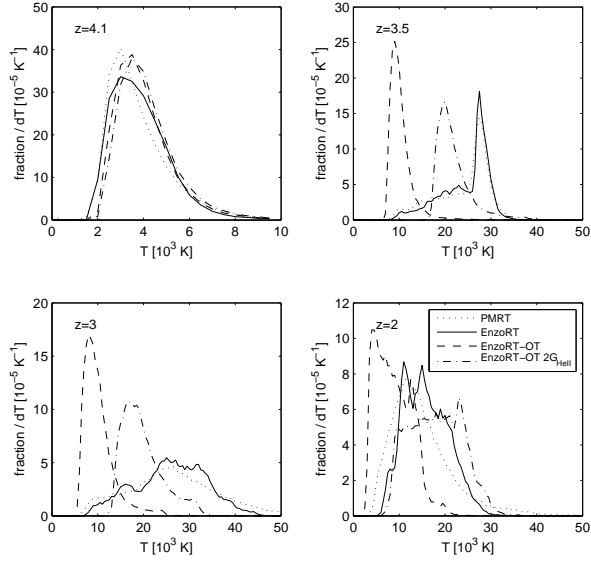


Figure 24. Temperature distributions at $z = 4.1, 3.5, 3.0$ and 2.0 for computation using *Enzo* with radiative transfer (solid lines), *Enzo* in the optically thin limit (dashed lines), *Enzo* in the optically thin limit but with the HeII heating rate doubled (dot-dashed lines), and the pseudo-hydrodynamics RT code PMRT (dotted lines). Note the smaller temperature scale at $z = 4.1$, prior to HeII reionization.

$\rho/\langle\rho\rangle < 1$. At $z = 2$, good agreement is found between the *Enzo* RT and boosted HeII heating rate simulations for underdense structures, but the latter produces too high temperatures for overdense structures. The distribution from the optically thin *Enzo* simulation agrees well with the others at $z = 4$, but once HeII reionization commences, the temperatures are systematically too low.

The temperature distributions of the *Enzo* with radiative transfer and the PMRT runs are very similar, as shown in Fig. 24, which may be expected from the overall agreement in the density-temperature distributions. By $z = 2.0$, however, the PMRT simulation systematically underestimates the temperatures by $3 - 5 \times 10^3$ K. Most of the volume is too cold in the *Enzo* simulation with the boosted HeII heating rate for $3.0 \leq z \leq 3.5$, although a tail of warmer temperatures results from overdense material, as shown in Fig. 23. By $z = 2$, these temperatures extend the distribution towards too high values compared with the RT simulations.

6.3 Spectral signatures

To assess the observational impact of the physical differences arising from the hydrodynamical response of the gas compared with the pseudo-hydrodynamics simulation on the Ly α forest, sample spectra are drawn from the *Enzo* and PMRT simulations, and the absorption features fit. As is clear from Figs. 8 and 9, reionization induces substantial peculiar velocities to the gas that a pseudo-hydrodynamics scheme like PMRT is unable to reproduce. The differences are small compared with the peculiar velocities present due to large scale flows, as is evident by a comparison with the full peculiar velocity distribution shown by the rightmost curve in Fig. 9. The comparison between the *Enzo* run with radiative transfer and the run without reionization, however, suggests

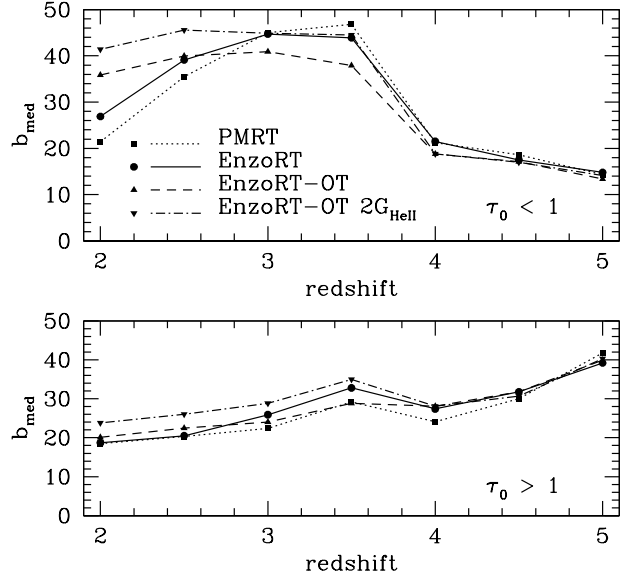


Figure 25. Evolution in the median Doppler parameter for the computation using *Enzo* with radiative transfer (solid lines), *Enzo* in the optically thin limit (dashed lines), *Enzo* in the optically thin limit with the HeII heating rate doubled (dot-dashed lines), and the pseudo-hydrodynamics code PMRT (dotted lines). (Top panel) Results for lines optically thin at line centre. (Bottom panel) Results for lines optically thick at line centre.

differences as great as 10 km s^{-1} are produced, with differences of $1 - 2 \text{ km s}^{-1}$ typical. These should be reflected in the line widths, although the differences in gas temperature will affect the line widths as well. For a pre-HeII ionization temperature of 5000 K , a temperature boost to 20000 K will double the thermal line width, increasing it to 18 km s^{-1} . The additional broadening due to the increase in peculiar velocity will augment the increase due to thermal broadening by at most only a few kilometres per second. In comparison with the optically thin reionization simulation, the additional peculiar velocities induced when radiative transfer is included add negligibly to the broadening.

The evolution of the resulting median Doppler parameters is shown in Fig. 25. The values generally agree well for the absorption lines optically thick at the line centre (bottom panel), although with deviations of $\sim \pm 4 \text{ km s}^{-1}$ from the *Enzo* RT simulation. The optically thin *Enzo* simulations agree best with the RT run at $z > 3$, with the simulations with the boosted and non-boosted HeII heating rates bracketing the RT simulation, but producing too broad features by $z < 3$, where the PMRT simulation gives near perfect agreement.

By contrast, the PMRT simulation recovers the median Doppler parameters for the absorption lines optically thin at line centre for $z > 3$. These weaker lines arise from gas too rarefied to maintain atomic thermal balance with the photoionization heating rate, so that including the temperature heating due to radiative transfer is required. The good agreement with the *Enzo* RT simulation results shows that hydro-

dynamical feedback contributes little additional broadening to the lines. The optically thin **Enzo** simulation produces lines that are $\sim 5 \text{ km s}^{-1}$ too narrow at $3 < z < 3.5$. Boosting the HeII heating rate recovers the median Doppler parameter well for $3 < z < 3.5$, but overheats the gas at lower redshifts. At $z < 3$, adiabatic cooling in the PMRT simulation produces features that are too narrow compared with the **Enzo** RT simulation. None of the approximate methods provides an adequate description of the absorption line widths over the full redshift range of interest.

7 CONCLUSIONS

A radiative transfer module based on the method of Tittley & Meiksin (2007) was incorporated into the gravity-hydrodynamics code **Enzo** to investigate the impact of HeII reionization on the structure of the IGM. The RT module is specifically designed to account for the heating by the hardening of the radiation field on passing through inhomogeneities in the density field, crucial for capturing the heating due to hard sources like QSOs. The combined code is able to capture the hydrodynamical feedback following the reionization of both hydrogen and helium.

A simulation of a plane-wave ionization front sweeping across a volume $25 h^{-1} \text{ Mpc}$ (comoving) on a side, representing a characteristic I -front produced by photoionizing sources, was performed. The source spectrum was initially a starburst, transforming gradually into a QSO spectrum $f_\nu \sim \nu^{-0.5}$ over the redshift interval $3 < z < 4$ to represent the onset of HeII reionization by QSO sources. Simulations in the optically thin limit, one without and one with the HeII heating rate doubled, and an N -body based pseudo-hydrodynamics simulation with radiative transfer using PMRT, are performed with identical initial conditions to the **Enzo** radiative transfer simulation in order to examine how well results from these simpler approximate methods compare.

Substantial heating is introduced by HeII reionization, with temperatures exceeding those following HeII reionization in the optically thin limit by typically $10 - 20 \times 10^3 \text{ K}$. High temperatures, in excess of $35 \times 10^3 \text{ K}$, are produced in the “shadows” of overdense structures as the HeII is photoionized by a radiation field hardened on passing through the overdense structures. While peculiar velocities are boosted by $0.1 - 10 \text{ km s}^{-1}$ by $z = 3$ over a simulation with no HeII reionization, the differences compared with a simulation with HeII reionization in the optically thin limit are typically smaller than 1 km s^{-1} . The expansion of the gas following HeII reionization, however, plays an important role in curtailing the hardening of the radiation field by reducing the gas density in small haloes. As a result, the temperature-density relation is somewhat tighter and flatter compared with the corresponding PMRT simulation, for which no hydrodynamical response is accounted for. In rare regions, the temperature in dense regions when radiative transfer is included is lower than the corresponding **Enzo** simulation in the optically thin limit, a consequence of complete shadowing of HeII-ionizing photons by dense clumps in the radiative transfer computation.

The gas flows induced by HeII reionization alter the gas density field on large scales (several comoving megaparsecs

in extent), with density reductions by as much as 10–20 per cent. compared with a simulation without HeII reionization. In much smaller regions, the gas is pushed into structures with density increases of up to 50 per cent. Compared with a simulation with HeII reionized in the optically thin limit, the density changes are much reduced, with large scale reductions of ~ 5 per cent., and density enhancements of a few to several per cent. in complex density regions.

Because the dark matter is coupled gravitationally to the gas, displacements in the gas will produce displacements in the dark matter as well. Large scale coherent reductions in the dark matter density of up to 0.5 per cent. are found at $z = 3$, increasing to nearly 1 per cent. by $z = 2$. Small dense regions show enhancements in density by 0.2 per cent. at $z = 3$ to 1 per cent. at $z = 2$. The dark matter and gas density displacements may produce distortions of a few per cent. in the matter power spectrum on comoving wavenumber scales of $k > 0.5 h \text{ Mpc}^{-1}$.

The reionization of HeII has a substantial impact on the H I Ly α forest, as would be measured in the spectra of background QSOs. Synthetic spectra are drawn from the simulations and normalised according to measured values of the mean H I and HeII transmission values. The most conspicuous effect is on the broadening of the absorption features. As the Doppler parameter distribution may be measured to high accuracy in a given QSO spectrum, with a median Doppler parameter determined to a precision of $\sim 1 \text{ km s}^{-1}$ or better, the line widths are a potentially powerful means of constraining the HeII reionization process and the nature of the ionizing sources. (Alternative measures of the line shapes, such as discrete wavelet coefficients or the flux curvature, may similarly be sensitive probes of the reionization history.) The heating induced by radiative transfer, however, will affect the other flux-related statistics as well.

Compared with HeII reionization in the optically thin limit, the boost in temperatures when radiative transfer is included produces a larger fraction of weak H I absorption features with optical depths < 0.1 , and a smaller fraction of moderate optical depth systems with optical depths 0.1–0.6. This may be accounted for by the increase in the line widths and reduction in the neutral fraction at a given gas density due to the higher temperatures, as both tend to reduce the line centre optical depth of the absorption features. The modifications to the optical depths result in a shift in the pixel flux cumulative distribution, with a maximum difference between the cumulative distributions from the **Enzo** runs with and without radiative transfer of ~ 0.1 at $z = 3$, readily detectable in measured spectra.

The H I Ly α forest spectra are found to be fully resolvable into absorption features. The resulting H I column density distribution of the fit lines is somewhat broader when radiative transfer is taken into account compared with the optically thin simulation. Fewer narrow lines are found in the simulation with radiative transfer than without. The median Doppler parameter evolves little between $2.5 < z < 3.5$, with $b_{\text{med}} \simeq 35 \text{ km s}^{-1}$, but decreases to $b_{\text{med}} \lesssim 25 \text{ km s}^{-1}$ by $z = 2$. Dividing the absorption features into those optically thin and optically thick at line centre reveals a sharp difference in the evolution of the features. Those optically thick evolve slowly, increasing from $b_{\text{med}} \simeq 27 \text{ km s}^{-1}$ when HeII reionization begins at $z = 4.0$ to $b_{\text{med}} \simeq 33 \text{ km s}^{-1}$ at $z = 3.5$, then gradually diminishing to $b_{\text{med}} \simeq 19 \text{ km s}^{-1}$ at

$z = 2.0$. By contrast, the median Doppler parameter of the optically thin lines increases rapidly from $b_{\text{med}} \simeq 21 \text{ km s}^{-1}$ at $z = 4.0$ to $b_{\text{med}} \simeq 44 - 45 \text{ km s}^{-1}$ at $3.0 \leq z \leq 3.5$, then diminishes slightly to $b_{\text{med}} \simeq 39 \text{ km s}^{-1}$ at $z = 2.5$ and rapidly to $b_{\text{med}} \simeq 27 \text{ km s}^{-1}$ by $z = 2.0$. The median Doppler widths of the optically thick systems agree well with those measured. By contrast, the median values of the optically thin systems at $3 < z < 3.5$ substantially exceed those measured, suggesting either HeII reionization was imposed too late in the simulation, having just completed at $z \simeq 3$, or that the source spectrum is too hard. A previous PMRT simulation with HeII reionization initiated at $z = 5.0$ (Tittley & Meiksin 2007) produced a substantially lower peak temperature of $15 \times 10^3 \text{ K}$ by $z = 3.0$, cooler than found here by $10 - 20 \times 10^3 \text{ K}$. Cooler temperatures may thus be achieved if HeII reionization were substantially completed prior to $z = 3$, although this may be at tension with recent claims that HeII reionization extended to $z < 3$. The PMRT simulations also found cooler temperatures arose when a single power-law spectrum reionized both hydrogen and helium, so that the temperatures are sensitive to the amount of HeII reionization during the hydrogen reionization epoch. Clearly simulations allowing for a more complex HeII reionization history involving a range of source histories and spectra are required to fully match the data.

The PMRT simulation matches the median Doppler width of the optically thick absorbers in the *Enzo* radiative transfer simulation to an accuracy of 2 km s^{-1} at $z \geq 4$ and better than 0.5 km s^{-1} at $2 \leq z \leq 2.5$, but underpredicts the widths by as much as 3.5 km s^{-1} at intermediate redshifts. For the absorbers optically thin at line centre, the agreement is to better than 2 km s^{-1} for $3.0 \leq z \leq 5$, but underpredicts the widths by $\sim 5 \text{ km s}^{-1}$ by $z = 2.0$.

Doubling the HeII heating rate in an optically thin *Enzo* simulation produces a close match to the median Doppler parameter of the optically thin absorbers from the *Enzo* simulation with radiative transfer over $3.0 \leq z \leq 3.5$, agreeing to within 0.6 km s^{-1} . But by $z = 2.0$, the median Doppler parameter is overpredicted by $\sim 15 \text{ km s}^{-1}$. The Doppler parameters of the absorption systems optically thick at line centre are overpredicted by $2-6 \text{ km s}^{-1}$ over $2.0 \leq z \leq 3.5$. The approximate methods are thus unable to reproduce the correct amount of broadening to the accuracy with which it is measured over the full range of redshifts for which the forest may be observed in high resolution, high signal-to-noise ratio spectra.

Just as absorption features may fully account for the pixel flux distribution in Ly α , a line blanketing model accounts well for the evolution in the mean transparency of the IGM in higher order Lyman series lines. Effective optical depth ratios for the H I of $\tau_{\text{Ly}\beta}^{\text{eff}}/\tau_{\text{Ly}\alpha}^{\text{eff}} \simeq 0.36$ and $\tau_{\text{Ly}\gamma}^{\text{eff}}/\tau_{\text{Ly}\alpha}^{\text{eff}} \simeq 0.21$ are predicted at $z = 3.0$ from the *Enzo* radiative transfer simulation.

Radiative transfer through density inhomogeneities in the IGM results in a wide spread of HeII Ly α optical depths compared with H I even after HeII reionization has completed in the simulation at $z = 3$. A broad peak centred at $\tau_{\text{HeII}}/\tau_{\text{H I}} \simeq 105$ is found at $z = 3.0$, diminishing to 80 at $z = 2.5$ and 75 at $z = 2.0$.

As for the H I, the pixel flux distribution for HeII Ly α may be fully accounted for by absorption lines for $2.0 \leq z \leq 2.5$. At $z = 3.0$, however, the mean transmission is too

low for meaningful absorption line fitting to be performed. Matching to the corresponding H I absorption features results in a broad distribution of the column density ratio $\eta = N_{\text{HeII}}/N_{\text{H I}}$, with a peak of $\eta \simeq 130$ at $z = 2.5$, well matching, though somewhat narrower than, the distribution measured in the ultraviolet spectra of high redshifts QSOs. While the value for η at the distribution peak results from the rescaling of the relative H I and HeII ionization rates required to match the measured effective H I and HeII Ly α optical depths, the distribution width is produced by the simulation and suggests that much of the observed spread may arise naturally from the radiative transfer through an inhomogeneous IGM.

Comparison between the column density and optical depth ratios indicates a typical Doppler parameter ratio of $\xi = b_{\text{HeII}}/b_{\text{H I}} \simeq 0.4$, close to the thermally broadened limit of $\xi = 0.5$. A comparison based on well deblended, unsaturated systems with line centre H I optical depths $0.01 < \tau_0 < 0.1$ shows a range in Doppler parameter ratios peaking between $0.5 < \xi < 1.0$, the latter corresponding to the limit of velocity-broadened features.

Line blanketing accounts well for the higher order HeII Lyman transmission through the IGM as well. The simulations predict effective optical depth ratios of $\tau_{\text{Ly}\beta}^{\text{eff}}/\tau_{\text{Ly}\alpha}^{\text{eff}} \simeq 0.36$ at $z = 2.5$, in agreement with the measured value, and $\tau_{\text{Ly}\gamma}^{\text{eff}}/\tau_{\text{Ly}\alpha}^{\text{eff}} \simeq 0.20$ (currently unmeasured).

A range of models, allowing for multiple QSO sources turning on over a range of redshifts with a variety of luminosities, spectral shapes and lifetimes, would be required to accurately match the H I and HeII absorption data as measured in the spectra of high redshift background QSOs. The simulations presented here demonstrate that HeII reionization simulations including radiative transfer are required to fully exploit the growing body of high quality IGM data at both optical and ultraviolet wavelengths.

ACKNOWLEDGMENTS

The computations reported here were performed using the SUPA Astrophysical HPC facility and facilities funded by an STFC Rolling-Grant. E.T. is supported by an STFC Rolling-Grant. Computations described in this work were performed using the *Enzo* code developed by the Laboratory for Computational Astrophysics at the University of California in San Diego (<http://lca.ucsd.edu>).

REFERENCES

- Anderson S. F., Hogan C. J., Williams B. F., Carswell R. F., 1999, *AJ*, 117, 56
- Becker G. D., Bolton J. S., Haehnelt M. G., Sargent W. L. W., 2011, *MNRAS*, 410, 1096
- Bolton J., Meiksin A., White M., 2004, *MNRAS*, 348, L43
- Bolton J. S., Haehnelt M. G., 2007, *MNRAS*, 374, 493
- Bolton J. S., Haehnelt M. G., Viel M., Carswell R. F., 2006, *MNRAS*, 366, 1378
- Bolton J. S., Haehnelt M. G., Viel M., Springel V., 2005, *MNRAS*, 357, 1178
- Bryan G. L., Machacek M. E., 2000, *ApJ*, 534, 57
- Burles S., Tytler D., 1997, *AJ*, 114, 1330

- Davé R., Hernquist L., Weinberg D. H., Katz N., 1997, *ApJ*, 477, 21
- Daivsden A. F., Kriss G. A., Zheng W., 1996, *Nature*, 380, 47
- Fardal M. A., Giroux M. L., Shull J. M., 1998, *AJ*, 115, 2206
- Faucher-Giguère C.-A., Prochaska J. X., Lidz A., Hernquist L., Zaldarriaga M., 2008, *ApJ*, 681, 831
- Fechner C., Reimers D., Kriss G. A., Baade R., Blair W. P., Giroux M. L., Green R. F., Moos H. W., Morton D. C., Scott J. E., Shull J. M., Simcoe R., Songaila A., Zheng W., 2006, *A&Ap*, 455, 91
- Furlanetto S. R., Dixon K. L., 2010, *ApJ*, 714, 355
- Haardt F., Madau P., 1996, *ApJ*, 461, 20
- Heap S. R., Williger G. M., Smette A., Hubeny I., Sahu M. S., Jenkins E. B., Tripp T. M., Winkler J. N., 2000, *ApJ*, 534, 69
- Jakobsen P., Boksenberg A., Deharveng J. M., Greenfield P., Jędrzejewski R., Paresce F., 1994, *Nature*, 370, 35
- Kriss G. A., Shull J. M., Oegerle W., Zheng W., Davidsen A. F., Songaila A., Tumlinson J., Cowie L. L., Deharveng J.-M., Friedman S. D., Giroux M. L., Green R. F., Hutchings J. B., Jenkins E. B., Kruk J. W., Moos H. W., Morton D. C., Sembach K. R., Tripp T. M., 2001, *Science*, 293, 1112
- Madau P., Meiksin A., 1994, *ApJ*, 433, L53
- McQuinn M., Lidz A., Zaldarriaga M., Hernquist L., Hopkins P. F., Dutta S., Faucher-Giguère C.-A., 2009, *ApJ*, 694, 842
- Meiksin A., 1994, *ApJ*, 431, 109
- Meiksin A., 2005, *MNRAS*, 356, 596
- Meiksin A., Bryan G., Machacek M., 2001, *MNRAS*, 327, 296
- Meiksin A., Tittley E. R., Brown C. K., 2010, *MNRAS*, 401, 77
- Meiksin A., White M., 2001, *MNRAS*, 324, 141
- Meiksin A., White M., 2003, *MNRAS*, 342, 1205
- Meiksin A. A., 2009, *Reviews of Modern Physics*, 81, 1405
- Miralda-Escudé J., Rees M. J., 1994, *MNRAS*, 266, 343
- Reimers D., Fechner C., Hagen H.-J., Jakobsen P., Tytler D., Kirkman D., 2005, *A&Ap*, 442, 63
- Reimers D., Kohler S., Wisotzki L., Groote D., Rodriguez-Pascual P., Wamsteker W., 1997, *A&Ap*, 327, 890
- Schaye J., Theuns T., Rauch M., Efstathiou G., Sargent W. L. W., 2000, *MNRAS*, 318, 817
- Scott J. E., Kriss G. A., Brotherton M., Green R. F., Hutchings J., Shull J. M., Zheng W., 2004, *ApJ*, 615, 135
- Shull J. M., Tumlinson J., Giroux M. L., Kriss G. A., Reimers D., 2004, *ApJ*, 600, 570
- Shull M., France K., Danforth C., Smith B., Tumlinson J., 2010, *ArXiv e-prints*, 1008.2957
- Smette A., Heap S. R., Williger G. M., Tripp T. M., Jenkins E. B., Songaila A., 2002, *ApJ*, 564, 542
- Steigman G., 2007, *Annual Review of Nuclear and Particle Science*, 57, 463
- Syphers D., Anderson S. F., Zheng W., Meiksin A., Haggard D., Schneider D. P., York D. G., 2011, *ApJ*, 726, 111
- Syphers D., Anderson S. F., Zheng W., Smith B., Pieri M., Kriss G. A., Meiksin A., Schneider D. P., Shull J. M., York D. G., 2011, *ArXiv e-prints*, 1108.4727
- Telfer R. C., Zheng W., Kriss G. A., Davidsen A. F., 2002, *ApJ*, 565, 773
- Theuns T., Schaye J., Haehnelt M. G., 2000, *MNRAS*, 315, 600
- Tittley E. R., Meiksin A., 2007, *MNRAS*, 380, 1369
- Wolf C., Wisotzki L., Borch A., Dye S., Kleinheinrich M., Meisenheimer K., 2003, *A&Ap*, 408, 499
- Zheng W., Chiu K., Anderson S. F., Schneider D. P., Hogan C. J., York D. G., Burles S., Brinkmann J., 2004, *AJ*, 127, 656
- Zheng W., Kriss G. A., Deharveng J.-M., Dixon W. V., Kruk J. W., Shull J. M., Giroux M. L., Morton D. C., Williger G. M., Friedman S. D., Moos H. W., 2004, *ApJ*, 605, 631
- Zheng W., Meiksin A., Pifko K., Anderson S. F., Hogan C. J., Tittley E., Kriss G. A., Chiu K., Schneider D. P., York D. G., Weinberg D. H., 2008, *ApJ*, 686, 195
- Zuo L., 1992, *MNRAS*, 258, 36